VANDERBILT UNIVERSITY

A Final Report to the Department of Energy

Office of Basic Energy Sciences

Materials Science and Engineering Division

For grant number **DE-FG02-99ER45781**

Submitted September 2015

Hydrogen-bond Specific Materials Modification in Group IV Semiconductors

for the period of August 15, 1999 to October 31, 2010

Ultrafast Studies of Hydrogen and Related Defects in Semiconductors and Oxides

for the period of November 1, 2010 to October 31, 2013

Ultrafast Studies of Defects, Dopants and Buried Layers in Semiconductors

for the period of November 1, 2013 to March 31, 2015

by

N. H. Tolk[1] (PI), L. C. Feldman[1] (co-PI) and G. Luepke[2] (co-PI)

[1]Department of Physics and Astronomy, Vanderbilt University

6301 Stevenson Center, Nashville, TN 37235-1807, 615-322-2786

[2]Department of Applied Science, The College of William & Mary, Williamsburg, Virginia 23187

Technical Contact: norman.tolk@vanderbilt.edu

Research Area: Experimental Condensed Matter Physics

DOE Technical Contact: Dr. James Horwitz

Administrative point of contact: Eric Dye,

phone: 615-343-1710,

eric.dye@vanderbilt.edu

Project Closeout Report for the grant number DE-FG02-99ER45781

Table of Contents

I. Executive summary

Semiconductor dielectric crystals consist of two fundamental components: lattice atoms and electrons. The former component provides a crystalline structure that can be disrupted by various defects or the presence of an interface, or by transient oscillations known as phonons. The latter component produces an energetic structure that is responsible for the optical and electronic properties of the material, and can be perturbed by lattice defects or by photo-excitation. Over the period of this project, August 15, 1999 to March 31, 2015, a persistent theme has been the elucidation of the fundamental role of defects arising from the presence of radiation damage, impurities (in particular, hydrogen), localized strain or some combination of all three. As our research effort developed and evolved, we have experienced a few title changes, which reflected this evolution. Throughout the project, ultrafast lasers usually in a pump-probe configuration provided the ideal means to perturb and study semiconductor crystals by both forms of excitation, vibrational (phonon) and electronic (photon). Moreover, we have found in the course of this research that there are many interesting and relevant scientific questions that may be explored when phonon and photon excitations are controlled separately.

Our early goals were to explore the dynamics of bond-selective vibrational excitation of hydrogen from point defects and impurities in crystalline and amorphous solids, initiating an investigation into the behavior of hydrogen isotopes utilizing a variety of ultrafast characterization techniques, principally transient bleaching spectroscopy to experimentally obtain vibrational lifetimes. The initiative could be divided into three related areas: (a) investigation of the change in electronic structure of solids due to the presence of hydrogen defect centers, (b) dynamical studies of hydrogen in materials and (c) characterization and stability of metastable hydrogen impurity states under transient compression. This research focused on the characterization of photon and ion stimulated hydrogen related defect and impurity reactions and migration in solid state matter, which requires a detailed understanding of the rates and pathways of vibrational energy flow, of the transfer channels and of the coupling mechanisms between local vibrational modes (LVMs) and phonon bath as well as the electronic system of the host material. It should be stressed that researchers at Vanderbilt and William and Mary represented a unique group with a research focus and capabilities for low temperature creation *and* investigation of such material systems.

Later in the program, we carried out a vigorous research effort addressing the roles of defects, interfaces, and dopants on the optical and electronic characteristics of semiconductor crystals, using phonon generation by means of ultrafast coherent acoustic phonon (CAP) spectroscopy, nonlinear characterization using second harmonic generation (SHG), and ultrafast pump-and-probe reflectivity and absorption measurements. This program featured research efforts from hydrogen defects in silicon alone to other forms of defects such as interfaces and dopant layers, as well as other important semiconducting systems. Even so, the emphasis remains on phenomena and processes far from equilibrium, such as hot electron effects and travelling localized phonon waves.

This program relates directly to the mission of the Department of Energy. Knowledge of the rates and pathways of vibrational energy flow in condensed matter is critical for understanding dynamical processes in solids including electronically, optically and thermally stimulated defect

and impurity reactions and migration. The ability to directly probe these pathways and rates allows tests of theory and scaling laws at new levels of precision. Hydrogen embedded in model crystalline semiconductors and metal oxides is of particular interest, since the associated local mode can be excited cleanly, and is usually well-separated in energy from the phonon bath. These basic dynamical studies have provided new insights for example into the fundamental mechanisms that control proton diffusion in these oxides. This area of materials science has largely fulfilled its promise to identify degradation mechanisms in electronic and optoelectronic devices, and to advance solid oxide proton conductors for fuel cells, gas sensors and proton-exchange membrane applications. It also provides the basis for innovations in materials synthesis involving atomic-selective diffusion and desorption.

In this final report on DOE# DE-FG02-99ER45781, we will describe work performed in chronological order under three titles representing progress in the time intervals outlined.

II. Hydrogen-bond Specific Materials Modification in Group IV Semiconductors,

N. H. Tolk[1], L. C. Feldman[1], and G. Lüpke[2]

[1]Department of Physics and Astronomy, Vanderbilt University, Nashville, TN 37235
[2]Department of Applied Science, The College of William and Mary, Williamsburg, VA 23187

a) Study of localized vibrational modes of H related defects in Si and Ge,

Report for the Period August 31, 1999 – September 1, 2002

Light impurities in crystalline solids are seen to give rise to localized vibrational modes (LVMs) with frequencies above the phonon bands of the solid. LVM spectroscopy has been applied extensively to study isolated impurities and impurity complexes in crystalline solids, including ionic crystals and semiconductors from their spectral width. Here we report the first measurements of the lifetime of a LVM in a crystalline semiconductor [1]. The lifetime of the stretch mode of bond-center H in Si, H^{+}_{BC} at 1998 cm^{-1} is measured to be $\mathbf{T}_1$ = 7.8 +/- 0.2 ps by transient bleaching spectroscopy. Infrared absorption spectroscopy (IRAS) shows that the spectral width of the stretch mode nearly coincides with its natural linewidth in samples with low H concentrations, indicating that lifetimes of LVMs under such conditions can be estimated from their spectral width. Using this approach, we estimate the Si-H stretch lifetimes of a selection of structurally well-characterized defects. Lifetimes of Si-H stretch modes are found to be strongly dependent on the structure of the defects, ranging from 1.6 to at least 37 ps. The strong dependence of the lifetime on the atomic structure of the defect suggests that pseudolocalized modes or LVMs are involved in the vibrational relaxation of Si-H bonds of point defects in solids.

In the next stage of our research, we carried out the first experimental observation of isolated H in Ge [2]. In situ infrared absorption spectroscopy (IRAS) on Ge implanted with protons at lines at 745 and 1794 cm^{-1}, which originate from local vibrational modes (LVMs) of distinct H-related defects containing one H atom. Uniaxial stress measurements show that both defects have trigonal symmetry, which implies that the H atoms are located on a <111> axis. The properties of the 1794 cm^{-1} mode are essentially identical to those of the stretch mode of bond center H in Si, and we therefore assign it to this defect in Ge. On the contrary, the 745 cm^{-1} line has no Si analog. The experimental results strongly suggest that the 745 cm^{-1} line originates from an isolated H species, most likely negatively charged H located close to the tetrahedral site. Although predicted by theory more than a decade ago, the present work provides the first direct observation of this isolated H species in a semiconductor.

Our research was extended to a comprehensive study of the absorption line shape associated with the fundamental transition of the H-related stretch mode of bond-center hydrogen in crystalline silicon, which was measured as a function of temperature with infrared spectroscopy [3]. In addition to the shift in frequency and increase in linewidth usually observed for local vibrational modes in solids, the absorption line becomes asymmetric at elevated temperatures. A theoretical

model is developed, which describes the temperature-dependent line shape in terms of thermal fluctuations in the occupation number of a low-frequency mode coupled anharmonically to the stretch mode. The model successfully describes the shift, broadening, and asymmetry of the absorption line and gives new insight into the nature of the low-frequency mode. The mode has a frequency of 114 cm^{-1}, is twofold degenerate, and exhibits no isotopic shift when deuterium is substituted for hydrogen. It is assigned to a pseudolocalized, Si-related mode of bond-center hydrogen.

The lifetime of the first excited vibrational state of $H_{BC}^{(+)}$ in germanium was shown to be 15–23 ps, 2–3 times greater than the lifetime of $H_{BC}^{(+)}$ in Si [4]. The increased lifetime in Ge is attributed to a higher-order decay process, which probably involves a combination of phonons and PLM's. The lifetime of $H^{(-)}$ in Ge was found to be > 36 ps. The lifetime of the $H^{(-)}$ mode is much longer, indicating that the lifetime is strongly structure dependent and that the order of the process is not as important as previously assumed. The observed broadening and shift of the $H^{(-)}$ absorption peak with temperature in germanium can also be treated using the extended exchange model in the temperature range 25–80 K. This $H^{(-)}$ -related exchange mode was determined to have an activation energy of 77**6** cm^{-1} , but the degeneracy of the exchange mode could not be determined. As in the $H_{BC}^{(+)}$ case, no change in the exchange mode frequency was observed upon substitution with deuterium, which shows that the mode is Ge related. An enhanced theoretical understanding of the structure of the $H^{(-)}$ defect is required to predict the exchange mode principally involved in the dephasing process.

Relaxation and delocalization of vibrational energy in the condensed phase entails the energy redistribution into low-frequency vibrational degrees of freedom that are anharmonically coupled to the initially excited local mode. To elucidate this process, we carried out a systematic study of the vibrational lifetime of hydrogen (H) embedded in bulk silicon (Si) a classic example of well-studied local vibrational modes [5]. The low-temperature lifetime of H at the bond-center site in crystalline Si and other interstitial-like configurations is of the order of 10 ps, while the lifetime of vacancy-H configurations are 1–2 orders of magnitude greater. This disparity in measured lifetimes is unexpected based on simple theories and is yet unexplained. From our experiments, the lifetimes of the Si-H vibrational stretch modes of the H_2^* (2062 cm^{-1}) and HV-$VH_{(110)}$ (2072.5 cm^{-1}) defects in crystalline Si were measured directly by transient bleaching spectroscopy from 10 K to room temperature. The interstitial-type defect H_2^* was seen to have a lifetime of 4.2 ps at 10 K, whereas the lifetime of the vacancy-type complex HV-$VH_{(110)}$ is 2 orders of magnitude longer, 295 ps. The temperature dependence of the lifetime of H_2^* is governed by TA phonons, while HV-$VH_{(110)}$ is governed by LA phonons. This behavior is attributed to the distinctly different local structure of these defects and the accompanying local vibrational modes.

b) Vibrational Lifetime and Isotope Effects of Interstitial Oxygen in Silicon and Germanium,

Report for the Period August 31, 2002 – September 31, 2005

During this period, review articles were published based on our work involving vibrational dynamics [6]–[9].

Decay dynamics of local vibrational modes provides unique information about energy relaxation processes to solid-state phonon bath. In this work, the lifetimes of the asymmetric stretch mode of interstitial ^{16}O and ^{17}O isotopes in Si are measured at 10 K directly by time-resolved, transient bleaching spectroscopy to be 11.5 and 4.5 ps, respectively. A calculation of the three-phonon density of states shows that the ^{17}O mode lies in the highest phonon density resulting in the shortest lifetime. The lifetime of the ^{16}O mode in Ge is measured to be 125 ps, i.e., ~10 times longer than in Si. The interaction between the local modes and the lattice vibrations is discussed according to the activity of phonon combinations.

Interstitial oxygen (O_i) in silicon (Si) and germanium (Ge) is known to occupy a bridge position between neighboring Si or Ge atoms. The well-understood defect is ideal for studying vibrational relaxation mechanisms in semiconductors, which are important to elucidate properties such as diffusion and defect reactions involving oxygen impurities. Recently, McCluskey and coworkers [10] used hydrostatic pressure to bring the asymmetric stretch mode of $^{18}O_i$ in Si into resonance with a spatially extended mode and studied the resonant interaction between these two modes. The authors stated that the transition from a localized to an extended mode might be the first step toward decay into lattice phonons. However, little is known about the actual decay dynamics of the local vibrational mode (LVM) into lattice phonons.

Study of the vibrational lifetime and calculation of multi-phonon density of states provide a direct way to elucidate the interaction between silicon (germanium) phonons and oxygen LVMs. In the past, isotope substitution of the oxygen center with ^{16}O, ^{17}O, and ^{18}O has been useful for experimental understanding of oxygen-related LVMs in silicon (germanium). However, the full width at half-maximum (FWHM) of the asymmetric stretch mode of $^{17}O_i$ in Si (1109 cm^{-1}) is a factor of two larger than for the $^{16}O_i$ (1136 cm^{-1}) and $^{18}O_i$ mode (1085 cm^{-1}), a puzzle that has not been solved since 1995. The effect may be related to their vibrational lifetimes and to the coupling between the local modes and the lattice phonons.

In this research program, we performed the first measurements of the vibrational lifetimes of

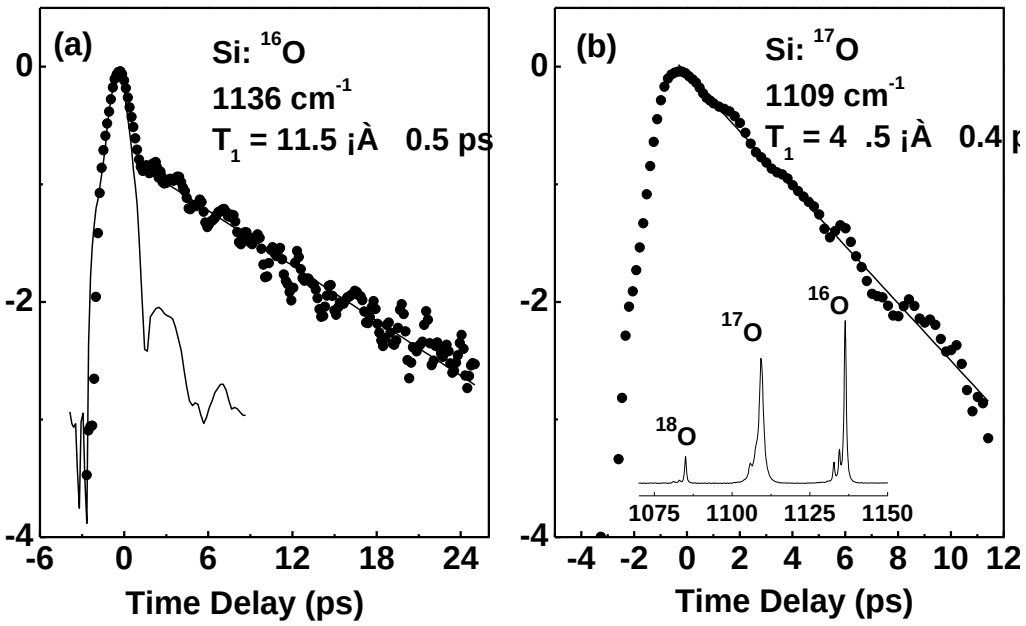

Figure 1 (a) The transient bleaching signal S_b decays exponentially with a time constant T_1 = 11.5 ± 0.5 ps for the asymmetric stretch mode of $^{16}O_i$ in Si at 10 K; (b) while T_1 = 4.5 ± 0.4 ps for $^{17}O_i$. The solid curve in (a) shows the S_b signal at a center frequency of 1123 cm^{-1}, i.e., between the two modes, decaying with the pulse duration of 1.7 ps. The inset in (b) shows the absorption spectrum of the asymmetric stretch mode of O_i isotopes in Si at 7.5 K

interstitial oxygen in silicon and germanium and their isotope effects. The lifetime of the asymmetric stretch mode of $^{16}O_i$ in Si is measured to be $T_1 = 11.5 \pm 0.5$ ps by transient bleaching spectroscopy, while for $^{17}O_i$ the lifetime is 4.5 ± 0.4 ps. This factor of 2.5 between their lifetimes coincides with the difference in their absorption linewidths. The combined three-phonon density of states is calculated to explain this isotope effect. The lifetime of the $^{16}O_i$ mode in Ge (861 cm^{-1}) is measured to be 125 ± 10 ps, much longer than in Si. The different vibrational decay channels of O_i isotopes in the two hosts are identified to explain the large difference in lifetimes. Our lifetime measurements show that oxygen absorption line broadening in silicon and germanium are homogeneous at liquid-He temperature. A float-zone grown silicon sample enriched with oxygen isotopes by diffusion is used for the lifetime experiment. The concentrations of ^{16}O, ^{17}O and ^{18}O isotopes are 20, 25 and 2.4×10^{16} cm^{-3}, respectively. The germanium sample contains isotopes ^{70}Ge, ^{72}Ge, ^{73}Ge, ^{74}Ge, ^{76}Ge, with relative (natural) abundances of 0.205, 0.274, 0.078, 0.365 and 0.079, respectively. The oxygen concentration of the Ge sample is 4.9×10^{16} cm^{-3}. The lifetime of the asymmetric stretch mode of interstitial oxygen isotopes is measured directly by transient bleaching spectroscopy. We use a low-temperature IR pump-probe setup. The traveling-wave optical parametric amplifier of superfluorescence (TOPAS) used in this experiment delivers pulses at 1-kHz repetition rate with a time duration of ~2 ps, spectral width of 15 ~ 20 cm^{-1}, and a pulse energy of 18 μJ at 1136 cm^{-1} and 1109 cm^{-1}, and 9 μJ at 861 cm^{-1}. The TOPAS beam is split into two parts, pump and probe, carrying 91% and 9% of the power, respectively. The pump excites a small fraction of the interstitial oxygen to the first excited state of the asymmetric stretch mode, which causes a transient increase in the transmission coefficient of the sample that decreases with time due to the decay of the excited mode. The transient bleaching signal S_b is monitored with the probe beam delayed in time with respect to the pump.

Figure 1 shows a semi-log plot of S_b vs time delay from the asymmetric stretch mode of $^{16}O_i$ and $^{17}O_i$ in Si at 10 K. Both decay profiles fit well to a single exponential function yielding a decay time $T_1 = 11.5 \pm 1$ ps for $^{16}O_i$, and $T_1 = 4.5 \pm 0.4$ ps for $^{17}O_i$. We could not measure the lifetime of the $^{18}O_i$ mode because of its low concentration. The solid line in Fig 1(a) is measured at a center frequency of 1123 cm^{-1}, i.e., between the two modes. The curve does not show any decay, but only the laser pulse with 1.7-ps pulse width. The TOPAS spectrum with a FWHM of 15 cm^{-1} is therefore narrow enough to distinguish between the vibrational modes of the oxygen isotopes in Si.

The inset of Figure 1 shows the infrared absorption spectrum of the asymmetric stretch mode of different oxygen isotopes measured from the Si sample at 7.5 K. The shape of an absorption line is generally given by the convolution of its homogeneous line shape with a function describing the inhomogeneous broadening. The FWHM of the $^{17}O_i$ line is ~1.2 cm^{-1}, while for $^{16}O_i$ and $^{18}O_i$ it is ~0.6 cm^{-1} at 7.5 K. The natural linewidth is given by

$$\Gamma_0 = 1/ 2\pi c T_1. \qquad (1)$$

The natural linewidth deduced from the lifetime is 1.12 cm^{-1} for $^{17}O_i$, and 0.44 cm^{-1} for $^{16}O_i$. Our results measured in the time domain are consistent with those in the frequency domain, which shows that the absorption lines of interstitial oxygen are homogeneously broadened in crystalline silicon at low temperature. We can therefore deduce the lifetime of the $^{18}O_i$ mode from the linewidth according to Eq. (1). The lifetime is ~10 ps, close to that for $^{16}O_i$.

The difference (factor of two) between the linewidths of $^{17}O_i$ compared with $^{16}O_i$ and $^{18}O_i$ is also observed in their lifetimes. An accidental resonance of the asymmetric stretch mode of $^{17}O_i$ with another excitation was proposed to explain this effect. The asymmetric stretch mode of O_i lies in the three-phonon continuum of Si. The interaction between LVMs and lattice vibrations is crucial to understand the decay into phonons which has been studied theoretically by Nitzan and coworkers. The decay rate (inverse lifetime) can be expressed as:

$$\frac{1}{T_1} = 2\pi \sum_{\{\nu\}} |\, G_{\{\nu\}} \,|^2 \; n_{\{\nu\}} \rho_{\{\nu\}} \,, \qquad (2)$$

where each channel $\{\nu\}$ is characterized by the set $\{\omega_1, \omega_2, \ldots, \omega_{N\nu}\}$ of accepting mode frequencies. Energy is conserved in the decay process, $\omega = \sum_{j=1}^{N_\nu} \omega_j$, where ω is the frequency of the LVM. The decay rate of each channel is given by the coupling strength $G_{\{\nu\}}$ of the channel, the function $n_{\{\nu\}}$ describing its temperature dependence, and the compound many-phonon density of accepting states $\rho_{\{\nu\}}$. In the low-temperature limit, the decay rate reflects spontaneous decay into N_ν accepting modes and $n_{\{\nu\}} \cong 1$. $\rho_{\{\nu\}}$ can be expressed in terms of a convolution of single phonon densities of states

$$\rho_{\{\nu\}} = \int dE_1 \int dE_2 \ldots \int dE_{N-1} \rho_1(\hbar\omega - E_1)\rho_2(E_1 - E_2)\cdots\rho_N(E_{N-1}) \,. \qquad (3)$$

Figure 2 (a) shows the three-phonon density of states for Si calculated by straightforward convolution of the one-phonon density of states according to Eq. (3). The one-phonon density of states was obtained from *ab initio* calculations, which are very reliable. The $^{17}O_i$ mode happens to fall right on the peak of the 2TO + 1TA phonon combination, whereas the $^{16}O_i$ and $^{18}O_i$ mode are on both sides with smaller combined phonon densities. High phonon density corresponds to a short lifetime. The ratio of the phonon densities at the frequencies of the $^{17}O_i$ and $^{16}O_i$ mode is ~ 1.3, which is smaller than the ratio of the lifetimes (~ 2.5). The difference of the phonon density provides a satisfactory explanation for the difference of the lifetimes. In a full treatment of vibrational relaxation by anharmonic coupling between LVM and lattice phonon modes, one should consider modifications introduced by the distortion of the lattice because of the impurities, which may affect the phonon density of states locally. Kato and coworkers [11] reported a surprisingly large effect of Si isotopic mass disorder on the linewidth of the asymmetric stretch mode of $^{16}O_i$, which cannot be explained well by their calculations. The linewidth of this mode in quasi-mono-isotopic (qmi) ^{29}Si and ^{30}Si samples are narrower than those in natural Si and ^{28}Si. This can be explained by the isotopic shift of the phonon frequency rather than the isotopic mass disorder.

Passing from ^{28}Si to ^{30}Si, the phonon frequency will shift to a lower wave number, which results in lower phonon densities for ^{29}Si and ^{30}Si than for natural Si at the frequency of the $^{16}O_i$ mode. Our lifetime measurements indicate that the decrease in phonon density results in longer decay times, which corresponds to narrower linewidths.

The isotopic mass disorder contributes little to the broadening of the linewidth, but will affect the phonon spectrum. Further insight into the vibrational dynamics of the O_i defect can be gained by studying the lifetime of the asymmetric stretch mode in germanium. At very low temperature, the $^{16}O_i$ mode at 862-cm^{-1} exhibits a vibration-rotation spectrum with many sharp lines within a 5-cm^{-1} range because of the Ge isotope effect and of the rotational structure (Figure 3).

The corresponding absorption linewidths are much smaller in Ge (~0.04 cm^{-1}) than in Si (~0.6 cm^{-1}). The lifetime of the asymmetric stretch mode is measured to be T_1 = 125 ± 10 ps at 10 K (Figure 3). Since the absorption lines of the $^{16}O_i$ mode for different Ge isotopes are very close, our laser pulses can measure only an average lifetime. This corresponds to an average linewidth of 0.04 cm^{-1} in good agreement with infrared absorption measurements. This indicates again that at low temperature and low defect concentration the $^{16}O_i$ mode in Ge is dominated by the natural linewidth, consistent with lifetime studies of hydrogen-related defects in silicon.

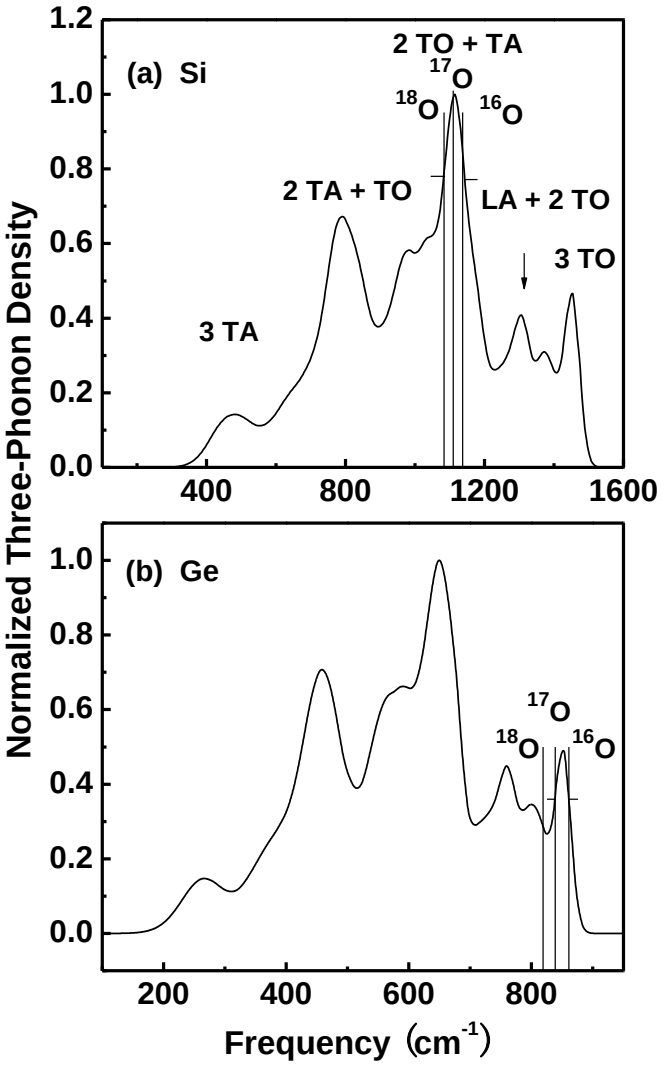

Figure 2 Normalized three-phonon density of states in (a) Si and (b) Ge at 0 K. (a) The asymmetric stretch mode of $^{17}O_i$ coincides with the highest three-phonon density in Si, whereas the $^{16}O_i$ and $^{18}O_i$ modes are on both sides of the 2TO + 1TA phonon peak. (b) In germanium, the $^{16}O_i$ and $^{17}O_i$ modes lie on the peak of the 3TO phonon density, whereas the $^{18}O_i$ mode coincides with a 2TO + LO phonon process.

To elucidate the long lifetime of the asymmetric stretch mode of $^{16}O_i$ in Ge requires knowledge of the decay channels and phonon density of states. The 862-cm^{-1} mode falls into the three-phonon continuum since the cut-off frequency of phonons in Ge is 306 cm^{-1}. Figure 2(b) shows the calculated three-phonon density of states in Ge similar to the one of Si. The $^{16}O_i$ mode falls on the 3TO phonon peak in Ge while it coincides with 2TO + TA phonon processes in Si. The difference in phonon density between the two peaks is only a factor of 2~3, which is not enough to explain the large difference in lifetimes. Since the decay channel is different for the two hosts, it is necessary to account for the coupling constant $G_{\{v\}}$, representing the strength of the interaction between the local mode and the accepting modes.

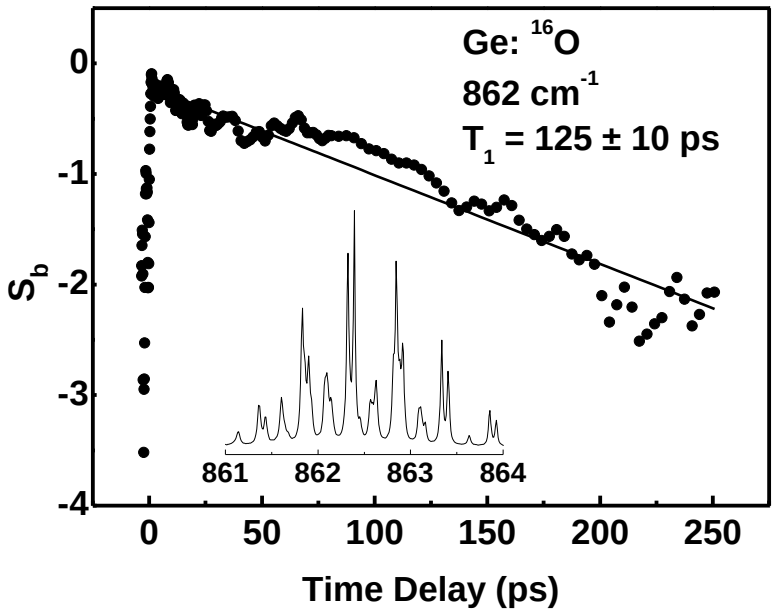

Figure 3 The transient bleaching signal S_b decays exponentially with a time constant T_1 = 125 ± 10 ps for the asymmetric stretch mode of $^{16}O_i$ in Ge at 10 K. The inset shows the corresponding absorption spectrum in Ge at 7.5 K.

Table I. Three-phonon processes in Si and Ge close to the frequency of the asymmetric stretch mode of interstitial oxygen. The infrared activity M is also listed.

Activity (M)	Phonon Combinations	Frequency (cm^{-1})
	Silicon	
3	TO(X)+O(Γ)+TA(X)	1129
6	TO(L)+O(Γ)+TA(L)	1122
3	2TO(L)+TA(X)	1134
6	TO(L)+TO(X)+TA(L)	1071
2	2TO(X)+TA(X)	1078
	Germanium	
1	2TO(X)+O(Γ)	856
3	2TO(L)+O(Γ)	888

The asymmetric stretch mode of interstitial oxygen in Si and Ge has A_{2u} symmetry, which is infrared active in the D_{3d} point group of the O_i defect. The three-phonon combinations must contain A_{2u} symmetry, or otherwise the decay channel is not allowed. The infrared dipole operator whose irreducible representation in the O_h group is Γ_{15}, can be reduced to A_{2u} + E_u

symmetry in the D_{3d} group, since D_{3d} (group of L in the diamond structure) is a subgroup of O_h. So we need to look into the infrared activity of three-phonon processes in the diamond structure. Table I lists the combinations of 2TO + TA phonons in Si and 3TO phonons in Ge which are infrared active. Activity (M) is the coefficient of $\Gamma_{15'}$ in the reduction of the direct sum of symmetry elements of three-phonon combinations. Larger M corresponds to a more infrared active three-phonon process. Table I shows that the combinations of 2TO + TA phonons are more IR-active than 3TO phonon processes. The interaction will be stronger between the A_{2u} local mode and the 2TO + TA phonons than with 3TO phonons. In addition, there are more channels for the A_{2u} mode to decay into 2TO + TA phonons, which results in a shorter lifetime of the oxygen mode in Si.

The oxygen isotope effect has been investigated also in Ge. A resonant broadening of the $^{17}O_i$ absorption line compared with $^{16}O_i$ and $^{18}O_i$ has not been observed in Ge, but the individual lines of $^{18}O_i$ are broader than those for $^{16}O_i$ and $^{17}O_i$. In Fig. 2 (b), we also plot the position of the $^{17}O_i$ and $^{18}O_i$ lines in Ge. The $^{16}O_i$ and $^{17}O_i$ lines coincide with the same peak (3TO phonons), both of them have the same decay channel and their three-phonon density of states is close. So they show the same linewidth in Ge. The $^{18}O_i$ mode in Ge may have different coupling constant since it decays into a different channel (2TO + LO phonons).

In conclusion, we have measured the vibrational lifetimes of the asymmetric stretch mode of oxygen isotopes in silicon and germanium. In silicon, the $^{17}O_i$ mode lies in the highest density of three-phonon states, which gives rise to a shorter lifetime (T_1 = 4.5 ps) than for the $^{16}O_i$ and $^{18}O_i$ modes (T_1 ~ 10 ps). We also measured the lifetime of $^{16}O_i$ modes in Ge, which show a much longer lifetime, T_1 = 125 ps, than in Si. We argue that the oxygen modes in Si decay into 2TO + TA phonons, while they decay into 3TO phonons in Ge. These phonon combinations have different infrared activities, which result in different coupling strengths and very different lifetimes. A more quantitative understanding of the vibrational energy relaxation and transfer channels in solids requires detailed knowledge of anharmonic coupling between LVM and lattice phonon modes and phonon density of states modified by impurities. The measured lifetimes presented here have great significance in elucidating the stability and diffusivity of impurities in semiconductors as well as complex formation and will generate renewed interest in the dynamics of energy dissipation from local modes into a phonon bath.

c) Hydrogen impurities and shallow donors in SnO_2

Report for the Period September 1, 2005 – October 31, 2008

Transparent conducting oxides have unusual but highly useful properties, combining transparency in the visible region of the spectrum with high electrical conductivity. SnO_2 is a prototypical transparent conducting oxide [12]. Recent theory finds that native defects are unlikely to be the source of conductivity. Instead, interstitial hydrogen [13] (H_i) and hydrogen at an oxygen vacancy [13] (H_O) have been predicted to be donors in SnO_2. H_i has been predicted to be mobile near room temperature whereas H_O has been predicted to be more thermally stable [13]. The understanding and control of unintentional donor centers in SnO_2 is of particular interest because theory also suggests that SnO_2 is a good candidate for p-type doping [13]. In the last year, we performed an IR absorption study of the various hydrogen centers in SnO_2, how they are produced, their annealing behavior, and their relationship to the free carriers that are introduced by hydrogen.

The SnO_2 samples used in our studies were bulk, rutile phase, single crystals that had been grown by the vapor transport method. To introduce additional hydrogen or deuterium, SnO_2 samples were placed in sealed quartz ampoules filled with H_2 or D_2 gas (2/3 atm at room temperature), annealed at elevated temperature, and quenched to room temperature in water to terminate the anneals. These anneals in H_2 or D_2 produced an opaque layer of Sn at the sample surface that was removed by lapping and polishing.

IR absorption spectra were measured with a Fourier transform infrared spectrometer. O-H and O-D vibrational modes were measured for SnO_2 samples at 4.2 K with an InSb detector. Samples were cooled with a continuous-flow cryostat. The absorption due to free carriers was measured in our SnO_2 samples to provide a contact-free method to probe the free-carrier concentration that is convenient for annealing experiments.

To probe the reactions and thermal stabilities of the various hydrogen-containing centers, annealing treatments were performed in a tube furnace with a flowing He ambient. The O-H lines and free-carrier absorption are not thermally stable for long storage times at room temperature. Therefore, samples were stored at 77K between measurements except for those experiments where the stabilities of the various hydrogen centers at room temperature were deliberately investigated.

Figure 4 shows IR spectra (4.2 K) of SnO_2 samples that contain H, D, or both H and D. Spectrum (i) was measured for an as-grown sample and shows a strong O-H line at 3261.5 cm^{-1}. Weaker lines are present at 3258.1 and 3272.0 cm^{-1}, respectively. Spectrum (ii) was measured for a SnO_2 sample that was annealed in a He ambient for 30 min at 500°C and quenched rapidly in D_2O. (D_2O was used to ensure that the quenching liquid was not the source of H.) The sample remained optically transparent after this treatment and showed an additional O-H line at 3156.0 cm^{-1}. Similar annealing treatments at 300°C and 700°C also produced the 3156.1 cm^{-1} line but with reduced intensity. Both spectra (i) and (ii) have flat baselines without any correction. The annealing treatment at 700°C in a He ambient also produced an IR spectrum with a flat baseline.

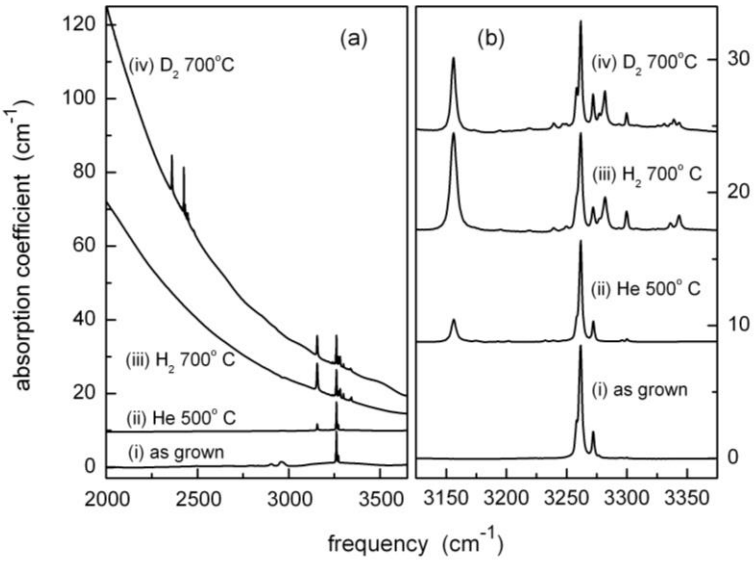

Figure 4 IR absorption spectra (T=4.2 K, resolution=1 cm^{-1}) for SnO_2 samples that had been annealed (30 min) in the ambient and at the temperatures that are indicated. The sample for spectrum (iii) had been preannealed at 1100 °C for 5 hours to remove H from the sample prior to an anneal in a deuterium ambient. (a) shows both the absorption due to free carriers and due to O-H and O-D centers. (An empty sample holder was used as the reference for these data.) (b) shows the IR lines in the O-H stretching region. These spectra were baseline corrected to remove the contribution from free-carriers.

Spectrum (iv) was measured for a SnO_2 sample that was annealed at 700°C for 30 min in a sealed ampoule containing H_2 gas (2/3 atm at room temperature). The heat treatment was terminated by quenching the ampoule in water. This anneal in H_2 gas caused the sample to partially decompose and damaged the sample surface, producing an opaque layer of Sn on the surface with a thickness of approximately 0.05 mm that was removed by lapping and polishing. The 3156.1 cm^{-1} line is introduced by this treatment with greater intensity than for spectrum (ii) along with additional lines at 3281.8, 3299.9, 3334.2, and 3343.2 cm^{-1}. This treatment in H_2 that severely damaged the SnO_2 sample surface also produced the broad low-frequency absorption that arises from the introduction of free carriers, similar to what was found previously for H in ZnO [14].

Spectrum (v) was measured for a SnO_2 sample that was annealed in a sealed ampoule containing D_2 gas (2/3 atm at room temperature) at 700°C for 30 min. This treatment also damaged the sample surface and produced several O-D lines that are the frequency shifted partners of the O-H lines seen in spectrum (iv). The dependence of the line intensities on annealing treatment to be shown below permitted the corresponding O-H and O-D lines to be identified. The ratios of H to D mode frequencies have values close to 1.34, consistent with their assignment to O-H and O-D stretching. Surprisingly, the treatment in D_2 gas also produced the complicated O-H line spectrum that was observed under H_2 annealing in spectrum (iv). The broad absorption due to free carriers in also seen in spectrum (v).

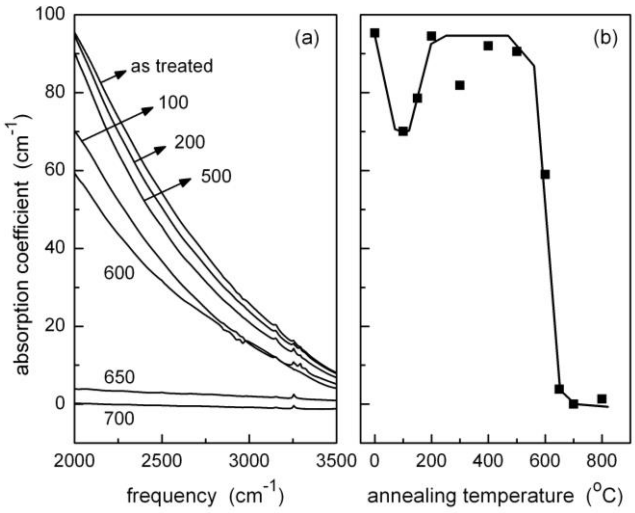

Figure 5 (a) Selection of free-carrier absorption spectra (room temperature, resolution=1 cm^{-1}) measured for a single-crystal SnO_2 sample. The sample was first annealed (30 min) at 700 °C in H_2 gas to introduce H. The sample was subsequently annealed in a He ambient at the temperatures shown. Anneals were terminated by a quench to room temperature in water. The reference spectrum for these data (not shown) was measured for the same sample following an anneal at 900 °C in a He ambient that was performed to remove H. (b) Difference in the absorption coefficients measured at 2000 cm^{-1} and 4000 cm^{-1} vs. the annealing temperature.

Samples used for spectra (i), (ii), (iv), and (v) were in their as-grown state prior to the heat treatment in the ambient that is indicated in Fig. 4. Spectrum (iii), however, was measured for a sample that had been preannealed at 1100 °C for 5 hrs in flowing He to remove hydrogen from the as-grown sample. This sample was then annealed in a sealed ampoule containing D_2 (2/3 atm at room temperature) at 700 °C for 30 min. Unlike for spectrum (v), in this case, only O-D lines were produced along with the absorption arising from free-carriers.

A series of annealing experiments has been performed to investigate the thermal stabilities of the free-carrier absorption and the various O-H and O-D centers. Figure 5(a) shows free-carrier absorption spectra that were measured at room temperature for a sample treated in H_2 gas following a series of subsequent heat treatments in a He ambient at the temperatures shown. Each anneal was terminated by a rapid quench to room temperature. The difference between the absorbances at 2000 cm^{-1} and 4000 cm^{-1} is taken to be a measure of the strength of the free-carrier absorption and is plotted as a function of the annealing temperature in Figure 5(b). The annealing of the free carrier absorption shows an interesting dependence on the heat-treatment temperature. Annealing the sample for 30 min at temperatures between 100 and 150 °C causes the free-carrier absorption to be reduced by nearly 25%. Anneals at temperatures $\geq$ 200 °C caused the free carrier absorption seen prior to annealing near 100 °C to be recovered. Upon further annealing at higher temperatures, the majority of the free-carrier absorption was finally eliminated by an anneal at 650 °C.

Figure 6(a) shows the stability of the free-carrier absorption after a sample that had been treated in an H_2 ambient (700ºC, 30 min) was "annealed" for long times at room temperature. The

strength of the free-carrier absorption was reduced by nearly 35% after 65 days at room temperature and was not reduced further after 108 days. Figure 4(b) shows the corresponding, baseline-corrected, O-H spectra. In this case, the intensity of the 3156.1 cm^{-1} line was nearly eliminated following storage for times of 65 days and longer. Over the same time period, the intensity of the 3261.5 cm^{-1} line was reduced by 24% while the intensities of the 3281.9 and 3343.2 cm^{-1} lines were increased. After the sample had been stored for 108 days at room temperature, it was re-annealed at 500 °C for 30 min in flowing He followed by a rapid quench. Following this heat treatment, the initial free-carrier absorption was recovered and the intensities of the 3156.5 and 3261.5 cm^{-1} lines were increased at the expense of the other O-H absorption lines in the sample. Furthermore, the total intensity of all of the O-H lines was found to be nearly constant for the various spectra shown in Figure 3, that is, for the as-treated sample, following the subsequent storage times at room temperature, and following heat treatment at 500 °C. This result suggests that the various O-H centers have IR lines with similar oscillator strengths and that these centers can be inter-converted into one another by the appropriate thermal treatments.

The annealing stabilities of the H-related donors in SnO_2 (Figure 5 and Figure 6) suggest that there are at least two H-related donors. The dip in the free-carrier absorption at 100 °C seen in the annealing data shown in Figure 5(b) suggests that there is a donor species that is not thermally stable at this temperature. There is also an additional shallow donor that is stable up to an annealing temperature of 650 °C where the majority of the free carrier absorption due to H disappears. The spectra shown in Figure 6(a) further support the conclusion that two donor species are present with different thermal stabilities. When a hydrogenated sample is held for 65 days at room temperature, the free-carrier absorption, measured in this case at 4.2 K, is reduced by 35%. This fraction accounts for the donor that is not stable at room temperature. The free-carrier absorption that remains is more thermally stable and does not decay appreciably for longer times at room temperature.

Our results for H in SnO_2 are similar to what has been found previously for H in ZnO where H_i, with an O-H vibrational line at 3611 cm^{-1}, and H_O both act as shallow donors. In ZnO that had been annealed in an H_2 ambient at 700 °C, approximately 85% of the donors that were formed were not thermally stable near room temperature and only 15% were stable up to near 500 °C. In ZnO, H_O was found to be formed in the near surface region of a sample treated in H_2 at temperatures near 700 °C. For SnO_2, we have introduced hydrogen with annealing treatments in H_2 that severely damage the sample surface. In these experiments, H_i and H_O are introduced deep into the bulk of the SnO_2 sample, and H_O is the dominant donor (≈65%) following hydrogenation. This result shows that the oxygen vacancies necessary for the production of the H_O donor center are introduced deep into the sample bulk by the damaging anneal in an H_2 ambient.

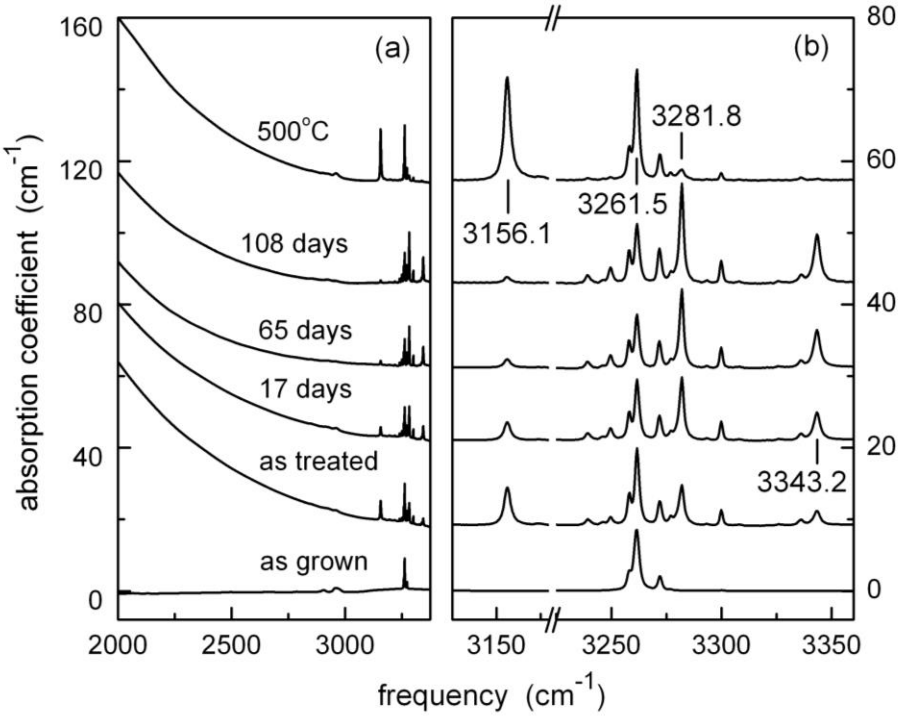

Figure 6 IR absorption spectra (T=4.2 K, resolution=1 cm^{-1}) for an SnO_2 sample that had been annealed (30 min) at 700 °C in H_2 gas to introduce H. The sample was subsequently held at room temperature for the times that are indicated. (a) shows both the absorption due to free carriers and due to O-H centers. (b) shows the IR lines in the O-H stretching region. These spectra were baseline corrected to remove the contribution from free-carriers.

The properties of H in single crystals of the transparent conducting oxide SnO_2 have been studied with IR spectroscopy. When H is introduced into SnO_2 by annealing in an H_2 ambient at elevated temperature, O-H vibrational lines are produced along with the low-frequency absorption that is characteristic of free carriers. An anneal in an H_2 ambient has been found to play a dual role, introducing both the hydrogen and the native defects that form shallow donors and O-H centers throughout the bulk of the SnO_2 sample. Furthermore, when an as-grown SnO_2 sample is annealed in a D_2 ambient, O-H centers and shallow donors are formed from electrically inactive hydrogen that was already present in the sample. To probe the relationship between H and the free carriers it introduces, the thermal stability of the free carrier absorption and its relationship to the thermal stabilities of the various O-H centers have been studied. Two H-related donors are found, one that is only marginally stable at room temperature and a second that is stable up to 600ºC. A vibrational line at 3156.1 cm^{-1} that was assigned previously by Hlaing Oo *et al* [15] to interstitial H has an annealing behavior that is consistent with its being the less stable donor species. The more stable donor is not seen by vibrational spectroscopy and has a thermal stability that is consistent with its being the H_O center (H trapped at an oxygen vacancy) that was predicted by theory [13] [15]**.**

d) O-H Stretch Mode and Proton Tunneling in Perovskite Oxides

Report for the Period September 1, 2005 – October 31, 2008

Crystalline oxides are ideal systems to investigate the energy dynamics of these omnipresent hydroxyl groups, since the associated stretch mode can be excited cleanly and is usually well separated in energy from the phonon bath. Moreover, many perovskite-structured oxides exhibit significant proton conductivity at elevated temperatures and quantum-mechanical tunneling has been suggested both experimentally and theoretically at sufficiently low temperatures. The interstitial proton or deuteron (D) in perovskite oxides has been found, to be bonded to an oxide ion, with the O-H axis oriented along the bisector of two oxygen nearest neighbors, as depicted in Figure 7(a). The proton forms a weak hydrogen bond with the second-nearest neighbor oxygen atom, and thus occupies a double Morse-type potential well (see Figure 7(b)). Proton conduction in these oxides is often attributed to the Grotthuss mechanism, consisting of sequential O-H···O transfer and O-H reorientation steps. Several theoretical studies have addressed the preferred sites, transition states, barrier heights and conduction pathways in these oxides using first-principles calculations or a molecular dynamics approach. However, none of these takes directly into account the vibrational dynamics and relaxation mechanisms of the O-H complex which can considerably affect the diffusion rate.

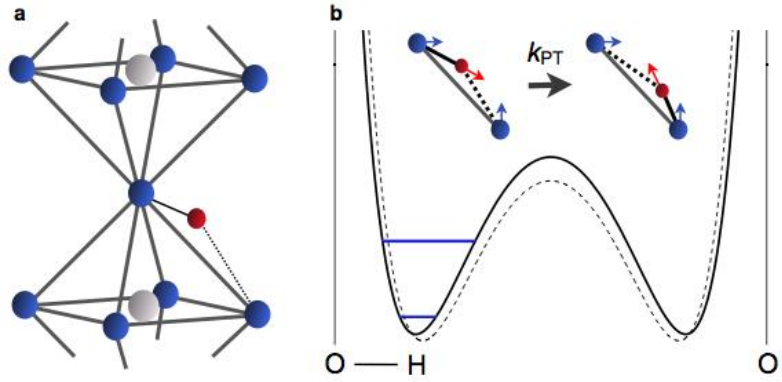

Figure 7 Fig. 1. The ionic configuration around the proton in a perovskite oxide. (a) The proton (red) moves throughout the oxygen (blue) octahedral network. (b) The potential energy diagram of the hydrogen atom, tunneling from one well into another. The vibrational ground and first excited state of the O-H stretch mode are shown. The red arrow in the inset corresponds to this stretching motion; the blue arrows indicate the O-O assist vibration.

In the last year, we reported experimental observation of excited-state proton tunneling as a decay channel of the O-H vibrational mode in the perovskite proton conducting oxide $KTaO_3$ [16]. The tunneling rate from the excited state is seven orders of magnitude larger than from the ground state in the proton conductor $BaCeO_3$ [17]. Identification of this new and unexpected relaxation channel provides new insights into the fundamental mechanisms that control proton diffusion in solids and suggests many important practical implications. For example, optically enhancing the proton conduction rate (either tunneling or hopping) in an oxide proton conductor could lead to increased efficiencies and lower operating temperatures in proton exchange devices such as fuel cell electrolytes, hydrogen sensors, and electrolyzers.

To investigate the vibrational lifetime and decay channels of the O-H (3487 cm^{-1}) and O-D stretch mode (2577 cm^{-1}) in $KTaO_3$ we use a picosecond infrared transient bleaching experiment described previously. High purity $KTaO_3$ single crystals are hydrogenated (deuterated) to a concentration of ~10^{17} cm^{-3} by annealing in H_2O (D_2O) vapor for 1 h (4 hrs for deuterium) at 1350 K. The time-resolved transient bleaching signal S_b of the O-H and O-D stretch modes exhibits unusually long lifetimes T_1 = 101±3 ps (at 70K) and 405±5 ps (at 100K), respectively (Figure 8). The latter represents one of the longest vibrational lifetimes so far reported for a hydrogen mode in a solid [18]. This observation for an interstitial hydrogen defect is remarkable considering that such long lifetimes have been reported only for hydrogen-vacancy complexes in covalent semiconductors (Si and Ge) where the open lattice structure reduces the coupling to the phonon bath [18].

Figure 8 shows that the lifetime of the O-D mode is significantly longer than the O-H mode at low temperatures. This large reverse isotope effect is unexpected based on the "frequency-gap law" [8], which predicts a shorter lifetime for the mode with the lower frequency and is inconsistent with the vibrational decay being due to the excitation of bulk phonons. Thus, for the O-H stretch mode, the most probable accepting channel is the bend mode as its frequency is localized above the phonon spectrum. We find the O-H bend mode at 1058 cm^{-1}, well above the highest bulk phonon frequency at ~850 cm^{-1}; and for the O-D bend mode a frequency of approximately 755 cm^{-1} has been estimated, a result that is consistent with the position of the combination mode and a small anharmonic shift. Since the excited local vibrational modes couple much stronger to other localized modes, we argue that the most likely decay channel of the O-H and O-D stretch mode involves three bend modes plus a phonon mode at 312 cm^{-1}.

We suggest that the high number of exchange modes and the weak coupling to the bending motion are responsible for the long lifetime of the O-H (O-D) stretch mode. This long lifetime seems to be quite common in the perovskite oxides as it shows consistently narrow linewidths, e.g. in $SrTiO_3$, and $LiNbO_3$. However, the O-H (O-D) linewidth of 0.12 (0.097) cm^{-1} observed in this work is not representative of the vibrational lifetime. Hence, these vibrational lifetimes cannot be determined from infrared absorption measurements.

Since both stretch modes most likely decay into three bend modes and a residual phonon around 312 cm^{-1}, one can expect the multi-phonon decay rate of these two modes to be very similar. The central question then becomes, what is the additional mechanism responsible for the different decay rate of the O-H stretch mode?

To address this issue, important information about the decay mechanism of the local mode is obtained from the temperature dependence of the vibrational lifetime. The lifetime of the O-H stretch mode exhibits very unusual temperature dependence, i.e., it decreases almost

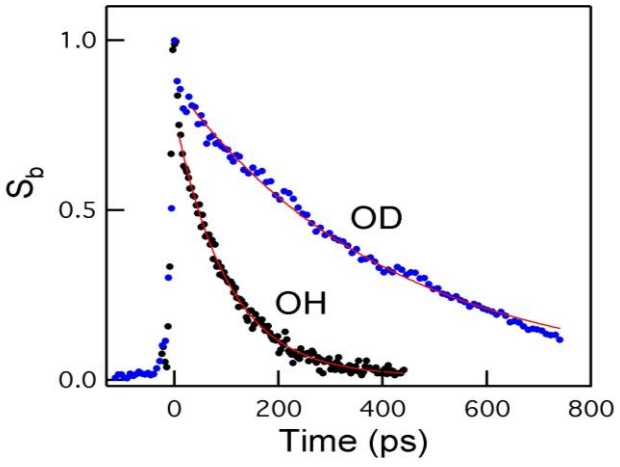

Figure 8 Transient bleaching signal S_b from the O-H (black) and O-D stretch mode (blue) as a function of time.

immediately at low temperatures with a very gentle slope. In contrast, the O-D mode shows typical behavior of a multi-phonon decay process, i.e., a broad plateau at low temperatures followed by a steep decline at elevated temperatures. Moreover, the large reverse isotope effect is most dominant at low temperatures. This clearly indicates that the decay mechanisms of the O-H and O-D stretch modes are very different. Since we expect the multi-phonon decay rate to be very similar for the two modes and the decay rate ($1/T_1$) is higher for the O-H mode, it is clear that an additional decay mechanism causes the shorter lifetime of the O-H mode.

We attribute this additional decay mechanism to a proton transfer process. The proton can hop over or tunnel through the potential barrier. Either process would lead to a large reverse isotope effect because of the difference in zero point energy. However, the former would require an activation energy of 0.89 eV and this thermally-activated process would vanish at low temperatures. This requirement is inconsistent with our data. Hence, we attribute the additional decay mechanism to proton tunneling. We estimate that the tunneling rate for deuterium is negligible, and therefore, the multi-phonon decay rate is given by $1/T_1$ of the O-D mode. Since both modes are expected to have approximately the same multi-phonon decay rate, we can estimate the proton tunneling rate as $k_{PT} = 1/T_{1(O\text{-}H)} - 1/T_{1(O\text{-}D)}$.

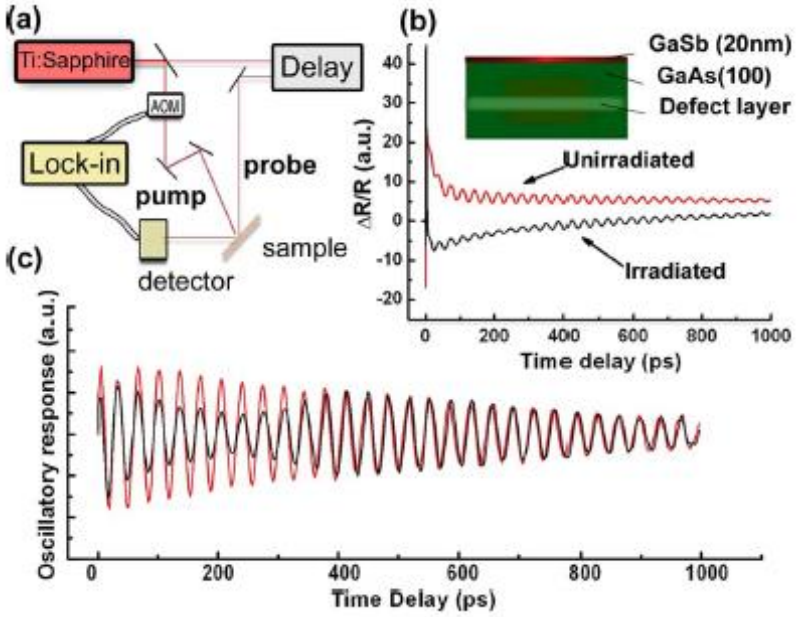

Figure 9 Showing the (a) experimental setup, (b) total time-resolved pump-probe optical response of the undamaged and damaged samples, and (c) the subtracted oscillatory responses displaying strong amplitude modulation observed in the damaged sample in the first 400 ps, as compared to the undamaged response.

e) Coherent Acoustic Phonon Interferometry

Report for the Period November 1, 2008 – October 31, 2010

In this work have utilized coherent acoustic phonon waves measure continuously varying defect concentrations in GaAs crystals as a function of depth, using near-band-gap photon energies to maximize the sensitivity to small perturbations in local optical properties caused by defects [19]. Defect concentrations in GaAs specimens were created through He^+ ion implantation over a wide range of doses, reliably creating damage profiles consisting of vacancy and interstitial defects, which can be simulated using the transport of ions in matter (TRIM) code.

Vanderbilt's 75 MHz Mira 900 Ti:sapphire laser with a pulse width of 120 fs was used in a standard time-resolved pump-probe setup with typical power ratios of 30:3 mW to optically

excite charge carriers in the GaSb layers. Figure 9(a) shows the experimental setup. Figure 9(b) shows the transient reflectivity response at probe wavelengths of λ=880 nm for an undamaged sample and a sample implanted with 325 keV He^+ at an irradiation dose of 3.5×1013 cm^{-2}. Both signals exhibit a typical fast initial rise due to electronic excitation and relaxation, with a superimposed with a long-lived oscillatory tail.

Figure 9(c) shows the subtracted oscillatory response, whose period can be described by $T=\lambda/(2nV_s\cos\theta)$, with oscillation period T, probe wavelength λ, refractive index n, and probe beam angle θ (here $\theta \approx 0$). Both samples exhibit amplitude attenuation due to natural attenuation of the probe light in the bulk GaAs, with absorption coefficient of α=210 cm^{-1} for λ=880 nm. The period and phase remain identical for both samples, with a clear difference in oscillation amplitudes. A strong amplitude modulation in the irradiated sample at early delay times of up to t_{delay}=350 ps is seen, corresponding to ~1.6 μm into the GaAs (for [100] GaAs, $Vs \approx$ 4.73 nm ps^{-1}). The two responses become concurrent after t_{delay}=350 ps, indicating that only a region near the surface was perturbed. The peak difference in amplitude ΔR_{max} between the samples is roughly 35% occurring at t_{delay}=240 ps or 1.1 μm. From the TRIM code, the simulated defect concentration at this point is estimated to be of the order of 5×10^{19} cm^{-3}.

To extract a profile of the influence of defect populations on the optical CAP response, the difference between the undamaged and damaged amplitudes is plotted versus depth. Figure 4 (a) plots the change in oscillation amplitudes $\Delta R/R$ for the sample irradiated at 325 keV as a function of depth, with the predicted total defect simulated by the TRIM code. The experimental and simulated data peak at the same depth, with a maximum amplitude difference near $\Delta R/R$=35% and a FWHM of about 750 nm.

In Figure 10(a) the experimental profile is broader than the simulated damage profiles, indicating a nonlinear dependence between the optical response and the influence of local defect concentrations. An experimental correlation changes in the optical response, and peak defect concentrations was established by varying irradiation doses, resulting in predicted peak defect concentrations between 5×10^{18} and 1×10^{21}. The optical CAP response for each sample was then collected, and the peak amplitude difference [e.g., 0.35 for the sample from Figure 10(a)], denoted as ΔR_{max}, was plotted versus the maximum simulated defect concentration [e.g., 5×10^{19} cm^{-3} in Figure 10(a)], denoted as Λ_{max} for each sample. The result is plotted in Figure 10(b) and displays a logarithmic dependence of ΔR versus defect concentration. This dependence may be used to transform the raw data [such as those in Figure 10(a)] into quantitative depth-dependent defect concentration profiles.

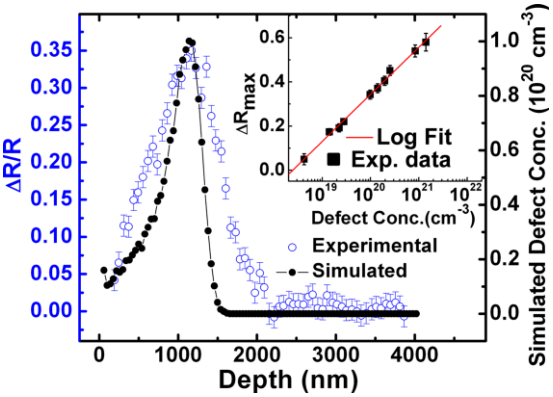

Figure 10 (a) Difference in oscillatory amplitudes between irradiated sample and undamaged samples, with comparison to the simulated peak defect concentration (solid black curve). (b) Experimental dependence of peak amplitude modulation ΔR_{max} vs peak defect concentration Λ_{max} as predicted from TRIM calculations. This dependence may be used to transform raw data in (a) into absolute defect concentration profiles.

Figure 11(a) shows the experimental defect concentration profile for a sample irradiated with 325 keV He^+ ions at a total dosage of 7×10^{13} ions/cm^2. The measured maximum defect concentration is near 1×10^{20} defects/cm^3, peaking near 1100 nm into the GaAs substrate. After calibration the FWHM of the experimental profile has been reduced to ~300 nm. The calibrated experimental profile agrees with simulations in peak depth, shape, and absolute defect concentration. Experimental defect profiles for other irradiation dosages yielded similar comparisons with simulations.

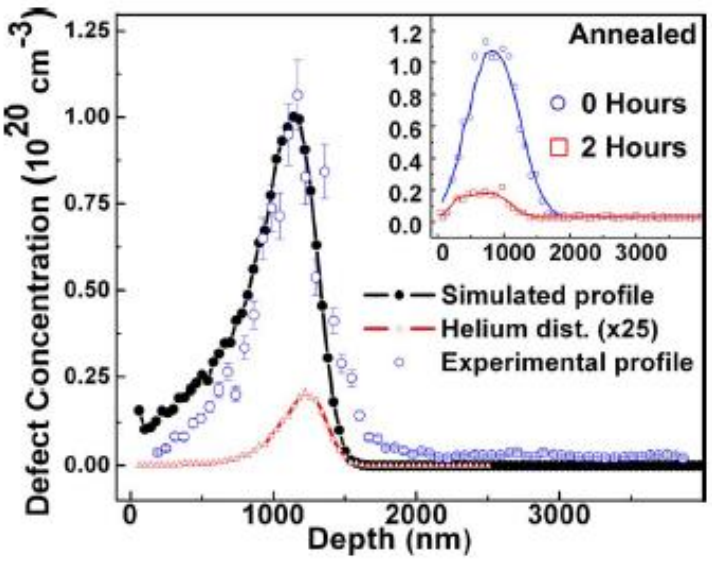

Figure 11 (a) Experimental defect concentration profile for a sample irradiated at 325 keV at a dosage of 7×10^{13} ions/cm^2. (b) Experimentally measured defect profiles before (blue) and after (red) 2 h of thermal annealing at 300 °C.

To test the effect of thermal annealing, another sample with an irradiated dose of 7×10^{13} ions/cm^2 was placed in an annealing furnace with an argon flow. The sample was annealed for 2 h at 300 °C. Figure 11(b) shows the experimental defect concentrations obtained before and after the annealing step. The annealed defect concentration is almost an order of magnitude lower than the unannealed sample.

The reduction in oscillatory amplitudes caused by radiation damage in the GaAs lattice can be attributed to (a) modification of the absorption coefficient induced by lattice defects or (b) changes through the derivative terms $\partial(n,k)/\partial E_g$. In Figure 11(c) the optical response of the damaged sample is seen to become concurrent with the undamaged sample after roughly t_{delay}=350 ps in both amplitude and period, indicating that any difference in the absorption coefficient in the damaged layer is below experimental resolution. Linear absorption measurements were performed, though no differences could be resolved between the two samples, likely due to the small thickness of the damaged layer compared to the bulk. Therefore, it can be concluded that amplitude modulation may be wholly attributed to changes in the derivative terms. This effect may be explained by the introduction of an impurity band during the irradiation process, which overlaps with the valence and conduction bands and leads to the formation of a band tail near the 1.43 eV GaAs electronic transition. Band tailing broadens the 1.43 eV band edge, which directly decreases the magnitude of the $\partial(n,k)/\partial E_g$ terms, as seen in the decrease in amplitude in the damaged region in Figure 11(c).

III. Ultrafast Studies of Hydrogen and Related Defects in Semiconductors and Oxides

Report for the Period November 1, 2010 – October 31, 2013

N. H. Tolk[1], L. C. Feldman[1], and G. Lüpke[2]

[1]Department of Physics and Astronomy, Vanderbilt University, Nashville, TN 37235
[2]Department of Applied Science, The College of William and Mary, Williamsburg, VA 23187

a) Studies of band-edge modification in radiation-damaged GaAs

We have applied the CAP technique to observe near-band edge optoelectronic modification in ion-irradiated GaAs. Disorder (e.g., structural defects) in a crystal lattice induces localized strain, and in turn modifies the optoelectronic structure in some volume surrounding the structural defects. In these experiments structural disorder was caused by Ne^{++} ion radiation, which creates a distribution of point defects and defect clusters that varies as a function of depth. CAP measurements were carried out systematically as a function of total Ne^{++} dose, and the change in the optical response was correlated with estimated number of point defects (as determined via channeling analysis and simulation). By understanding how optical modification evolved as a function of point defects, we established a model that estimated how many lattice points experience optical modification per unit disorder. Our conclusion, under the approximation the structural disorder caused by ion irradiation can be described as isolated point defects, was that nearly 700 neighboring atoms experience optical modification for each defect generated. Conceptually, this implies an "optical damage footprint" in a volume surrounding a point defect consisting of hundreds of atoms. This important observation gives an idea of the size scale over which bulk properties significantly deviate from the ideal crystal properties due to lattice disorder, and is particularly relevant in nanostructures where hundreds of optically modified atoms may account for a significant fraction of the entire structure. During this funding period, our studies of radiation damaged GaAs has been published [20]

b) Annealing Effect in Boron-Induced Interface Charge Traps in Si/SiO_2 Systems

We investigated annealing effects on the built-in interfacial DC electric field arising from boron-induced charge traps in Si/SiO_2 systems using a time-dependent SHG technique [21]. The observed initial time-dependent SHG signals suggest that the boron-induced charge traps are neutralized by annealing in non-oxygen environments (hydrogen, argon, and about 1 mTorr vacuum) at about 200 °C and 800 °C, and as well as 100 °C DI-water. Our data is most consistent with thermally assisted tunneling that modifies the charge states, but cannot fully rule out the role of desorption of surface adsorbate or boron remigration. Furthermore, we did not observe any recovery of the initial SHG signals in the annealed samples for several months. This research will lead to a significant improvement in our understanding of the role of boron impurities in silicon-based devices and will help enhance device reliability and performance.

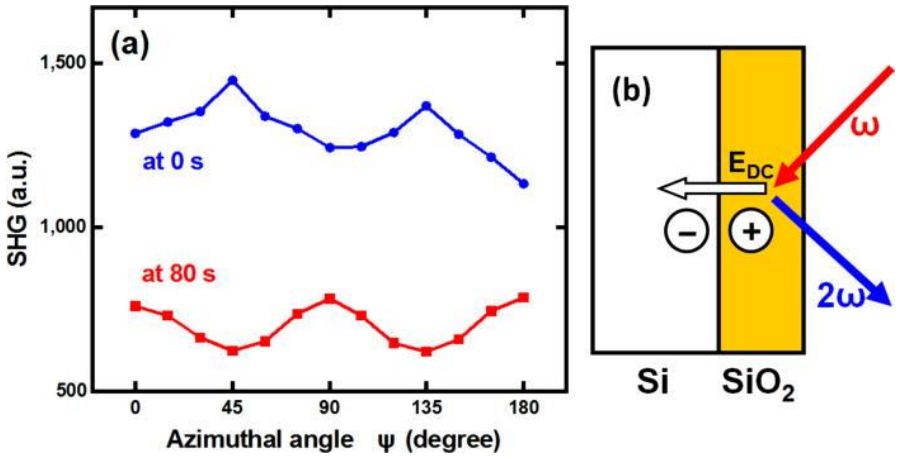

Figure 12 (a) Rotational anisotropic measurements of initial (at t = 0 s) and nearly saturated (at t = 80 s) SHG signals in an as-received boron-doped Si/SiO_2 sample with a laser beam power at 160 mW. $\Psi = 0°$ corresponds to that the incident plane is parallel to <110> silicon crystal plane. (b) Schematic diagram of SHG experiment and a boron-induced charge trap model.

c) Effect of Hydrogen Desorption Kinetics on Thermionic Emission from Polycrystalline Chemical Vapor Deposited Diamond

We measured the time-dependent thermal emission from polycrystalline CVD diamond films at temperatures between 600 and 800 °C [22]. The rate of decrease of emission behavior as a function of both time and temperature followed a first-order rate equation, similar to that observed for the desorption of hydrogen from diamond surfaces in previous studies. The rate constants obtained showed Arrhenius behavior with activation energy E_A = 1.23 eV, in agreement with reported values of the C-H bond energies on diamond (100) and (111) surfaces. Our results suggest that at low temperatures, hydrogenated diamond surfaces show high thermionic emission because the C-H surface dipole field induces negative electron affinity. At elevated temperatures, hydrogen desorbs, the dipole disappears, leading to positive electron affinity and reduced thermionic emission. Thus, our study demonstrates that the decline of the thermionic emission current from diamond at elevated temperatures is due to the first-order desorption of hydrogen from the surface C-H bond termination thereby altering the emission behavior as the hydrogen becomes depleted. This study provides a basis for further exploration into the relationship between H-bonding and thermionic emission and insight into methods to achieve stable, higher temperature TEC operation.

d) Ion Implantation-Induced Modification of Optical Properties in Single-Crystal Diamond Studied by Coherent Acoustic Phonon Spectroscopy

Ion implantation in crystals introduces defects into the lattice that modify local electronic wave functions and thereby modulate the opto-electronic properties of the material in ways that are not fully understood. In addition, ion implantation in diamond can transform the bonding characteristics of the lattice atoms, introducing significant strain in implanted crystals and, in some instances, causing surface swelling. Reliable fabrication of single-photon emitting centers and photonic devices in diamond will require a detailed understanding of the associated defects created within the lattice during the implantation process.

Single-crystal CVD diamond specimens were implanted with 1-MeV He^+ ions at fluences ranging from 10^{14} to 10^{16} cm^{-2} and analyzed using coherent acoustic phonon interferometry [23]. The coherent acoustic phonon response varies greatly with implantation fluence and provides depth-dependent information about the implantation defect-induced modification of diamond's optical characteristics. The results indicate a decrease in the real part of the refractive index, an increase in the imaginary refractive index, and a sign reversal of the photoelastic coefficient at higher levels of implantation damage. These studies provide insight into the application of ion implantation to the fabrication of diamond-based photonic devices.

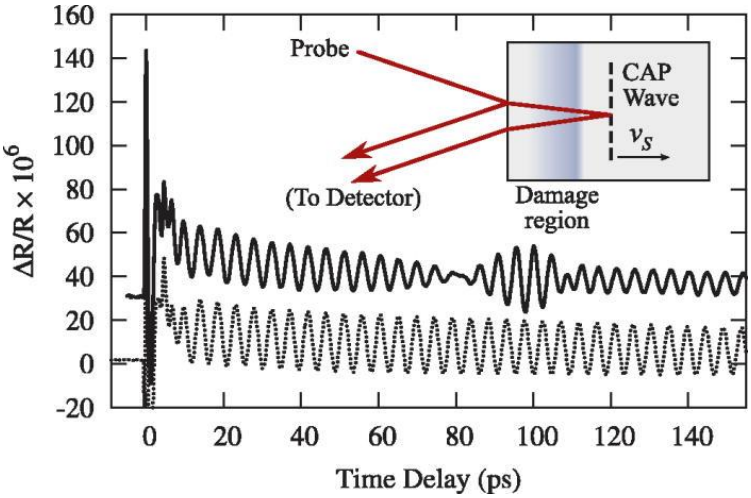

Figure 13 Typical pump-probe reflectivity responses for implanted (solid) and unimplanted (dotted) diamonds, vertically offset for clarity. Data are relevant to a sample implanted at a fluence of 3×10^{15} cm^{-2}. Inset: CAP experiment configuration showing strain-wave induced self-interference in the probe reflectivity. The CAP wave is generated by the optical pump (not shown).

IV. Ultrafast Studies of Defects, Dopants and Buried Layers in Semiconductors

Report for thePeriod November 1, 2013 – March 31, 2015

N. H. Tolk and L. C. Feldman

Department of Physics and Astronomy, Vanderbilt University, Nashville, TN 37235

a) Coherent Acoustic Phonon Interferometry applied to characterize optical properties of semiconductors

Accurately predicting the opto-acoustic response of a material like Si(100) allows one to utilize the full power of first-principles calculations and go beyond Maxwellian analytical or phenomenological models in order to model the PE response in defected or disorder materials. We have demonstrated excellent agreement between *ab initio* first-principles calculations and CAP spectroscopic measurements of the opto-acoustic response in Si(100) substrates [24]. Our calculation is shown to be consistent with the measured reflectivity behavior across the entire studied energy range of 1.4–3.5 eV (Figure 14), including the experimental observation that the CAP response increases by two orders of magnitude from 1.5 eV to 3.2 eV, the latter of which is in the vicinity of the $E_{\Gamma 1}$ direct band edge of silicon. We were also able to reproduce the time-domain reflectivity CAP response observed experimentally with good agreement. Our study motivates the extension to a theory-driven experimental study of dopant profiling, noninvasive nanometer-scale strain field analysis, and point-defect studies, among other applications.

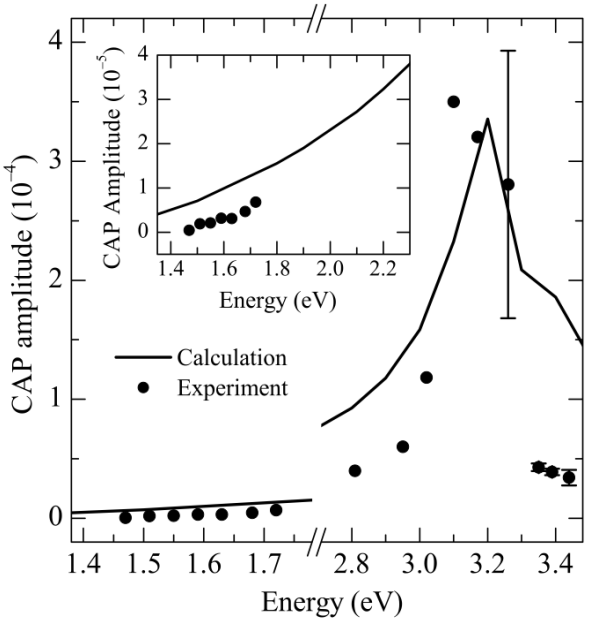

Figure 14 Comparison of theoretical (line) and experimental (dots) CAP amplitudes, showing overall agreement between theory and experiment. At some energies, more than one experimental result was obtained. In these cases, the mean value is presented, with error bars to indicate standard deviation. The inset presents an expanded view of the 1.4–2.3 eV range for the experimental and theoretical CAP responses.

b) Experimental and Theoretical Determination of the Optical Constants of Silicon Carbide (SiC)

Fundamental aspects of the hydrogen interaction with solids, e.g. the physisorption and chemisorption of hydrogen on the surface, hydrogen induced structural changes of solids as in metal insulator transitions, the occupation of interstitial sites, tunneling, interface and bulk states and the thermodynamics of hydrogen in the lattice, are all governed by the dynamics of the hydrogen bond. Ultrafast optical spectroscopy provides a powerful tool to characterize and manipulate hydrogen related dynamics with exquisite precision. This report explores hydrogen-solid dynamics and thus provides a base of understanding for applications ranging from hydrogen storage to semiconductor defect mediation to more efficient fuel cells and batteries to control of photovoltaics.

Knowledge of the rates and pathways of vibrational and electronic energy flow in condensed matter is critical for understanding dynamical processes in solids including electronically, optically and thermally stimulated defect and impurity reactions and migrations. The ability to directly probe these pathways and rates allows tests of theory and scaling laws at new levels of precision. Hydrogen embedded in model crystalline semiconductors and metal oxides is of particular interest, since the associated local mode can be excited cleanly, and is usually well-separated in energy from the phonon bath. Dynamical studies provide new insight into the fundamental mechanisms that control proton diffusion in these oxides. The science addresses issues of energy transfer and dissipation in solids, of fundamental importance to our understanding of solid-state properties and has numerous applications. This area of science is important to advance solid oxide proton conductors for fuel cells, gas sensors and proton-exchange membrane applications, to issues associated with hydrogen storage and to the atomic-level understanding of energy related electronic devices such as photovolatics. Our research provides the basis for innovations in materials synthesis involving atomic-selective diffusion and desorption.

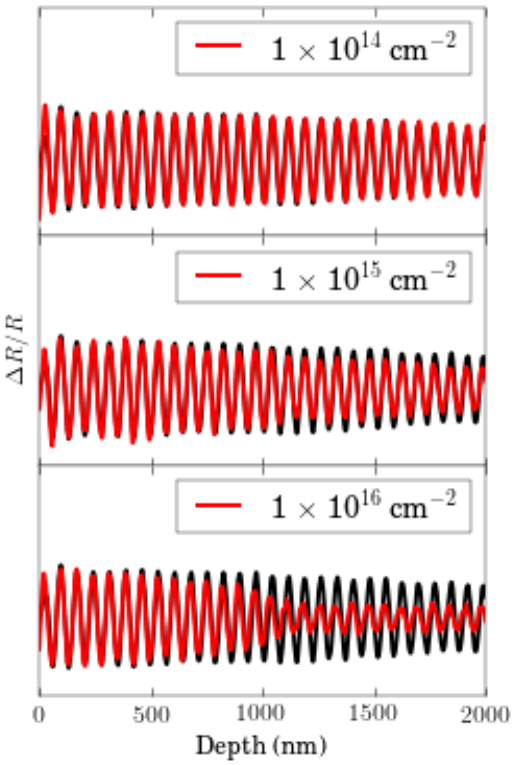

Figure 15 CAP oscillations in the pump-probe reflectivity signal of ion-implanted SiC specimens at multiple fluences (red lines). The black line behind each curve is the corresponding response for an unimplanted specimen.

In this work, we have utilized coherent acoustic phonon waves to measure continuously varying defect concentrations in SiC crystals as a function of depth, using near-band-gap photon energies to maximize the sensitivity to small perturbations in local optical properties caused by defects. Defect concentrations in SiC specimens

were created through H^+ ion implantation over a wide range of doses ($1x10^{14}$ cm^{-2} – $1x10^{16}$ cm^{-2}), reliably creating damage profiles consisting of vacancy and interstitial defects, which can be simulated using the transport of ions in matter (TRIM) code. CAP experiments were carried out at room temperature under the pump beam at 800nm and the probe beam at 400nm (3.1eV) that is just below the band gap of 4H-SiC (3.26eV).

Figure 15 shows CAP response for different fluences. The reduction in oscillatory amplitudes caused by radiation damage in the SiC lattice can be attributed to change in extinction coefficient due to hydrogen implantation.

c) Ultrafast Spectroscopic Characterization of ErAs:GaAs Nanoparticle Layers

We present here studies of the different relaxation regimes in the composite ErAs:GaAs system as this composite promises a variety of dynamic regimes highly dependent on ErAs nanoparticle density. This is a collaborative project with the Palmstrom group from the University of California, Santa Barbara.

Metal/semiconductor composites have hybrid electronic, dielectric and optical properties that may be controlled by manipulating the amount of metal in the semiconductor [25]. However, few metal/semiconductor systems have been studied with resonances in the infrared [26]. Composite systems like ErAs/GaAs may lead to optoelectronic devices by utilizing strong infrared resonant absorption. ErAs/GaAs offers an alternative to LT-GaAs for THz source and detector applications as it may be grown at normal GaAs temperatures; resulting in higher crystal quality, carrier mobility [27] and better control over photo-carrier lifetimes can be achieved [28]. ErAs nanoparticles embedded in GaAs lattices self-assemble during growth processes, act as fast recombination centers, and have transport characteristics that can be controlled by manipulating the growth parameters [29].

No known particle morphology studies exist for > 5% Er density. Previous TEM for lower densities showed slightly oblate particles 2.3:2.4 nm in diameter [29]. In pump-probe reflectivity experiments, we have observed evidence of polarization dependence, indicating the particles are no longer spherical. We propose to perform cross-sectional TEM to characterize particle shape and size and to correlate these characteristics with ultrafast response.
We are also investigating plasmon-phonon coupling in these materials as a function of nanoparticle density, wavelength, and injected photo-carrier density. We compared the coupling efficiency of the plasmon-phonon interaction to that of strain wave-injected phonons. Preliminary results indicate the plasmon-phonon coupling is significantly more efficient than strain wave for injection energies away from the band edge, both above and below.

The embedded ErAs particles alter the electronic states in the surrounding GaAs matrix, introducing localized states into the GaAs bandgap [29]. Evidence for an interface state 0.2eV above the Fermi level arising from the coordination and bonding differences has been observed where carriers in this state decay into the GaAs matrix [29].
Evidence for a surface-plasmon in the NIR has been observed for varying ErAs layer thicknesses and fill fractions [30]. The resonant absorption of the particles can be shifted by the growth conditions: it is possible to tune the resonant absorption from 1.3-2.5 um by altering the ErAs deposition [28]. Previous studies on similar ErAs embedded systems have shown a linear relationship in the magnitude of the absorption peak with increasing ErAs volume fraction up to

5% [30].

In superlattice structures with repeat units of ErAs/GaAs and GaAs, the presence of ErAs nanoparticles reduces the recombination time for photo-carrier excitation at energies above the bandgap. The photo-carriers are created in the GaAs matrix and captured by the ErAs islands, causing the initial transient decay and fast capture time on the order of two picoseconds, depending on the spacing between ErAs containing layers [31].

We have conducted preliminary experiments to characterize the ultrafast response of single layer ErAs:GaAs systems. Contrary to results obtained for superlattice systems, the single layers of embedded particles exhibit wavelength dependence in their relaxation times. The physical mechanism for this dependence is yet unclear, but our measurements indicate we may be observing a superposition of charge transfer processes characterized by different relaxation times.

We observe two distinct regimes of carrier relaxation in a time window of less than two picoseconds. The response of different densities of ErAs-incorporated systems are shown in Figure 16(a) with the two picosecond window relaxation timescales plotted in Figure 16(b). Previous studies in the THz range have provided evidence that these transients are photo-carriers generated in the GaAs and captured by the ErAs nanoparticles. We agree with this interpretation and further suggest there exist two distinct material regimes for such photo-carrier capture as can be seen in Figure 16(b). In addition, we observe the signature of carriers moving from the ErAs interface state *back* into the GaAs matrix for high density ErAs:GaAs, resulting in higher populations of cool carriers at longer time delays > 3 ps in Figure 1(a). The relaxation times for the cool carrier populations are plotted in Figure 16(c). As of yet, no time-resolved studies have reported carrier injection back into the GaAs matrix, however the differential conductivity study of the interface between ErAs and GaAs by the Palmstrom group reported evidence of such behavior [29]. The injection of extra carriers due to the presence of the ErAs/GaAs interface state appears to saturate around 7.5% ErAs density, although further studies need to be performed to verify.

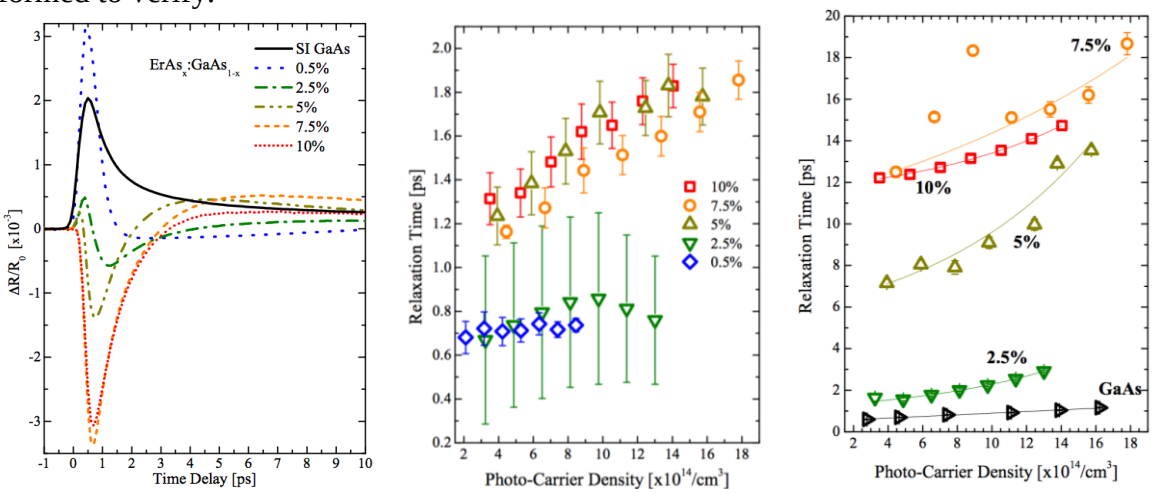

Figure 16: (a) Ultrafast pump and probe response of ErAs:GaAs composites at 800nm. (b) Photo-carrier density vs. relaxation time of response within first 2 ps. (c) Photo-carrier density vs relaxation time for cool carrier populations at times greater than 3 ps.

d) Effect of substrate on ultrafast relaxation dynamics of carriers and phonons in graphene

Graphene, the 2D allotrope of the carbon family exhibits impressive electron mobility and thermal conductivity and very strong electron-electron and electron-phonons interactions. The ease of integrating graphene on a variety of substrates makes graphene an excellent candidate for applications in electronics, photonics and optoelectronics [32]. However introducing a substrate will affect both the equilibrium and non-equilibrium dynamics and, inevitably influence the electrical and thermal properties of pristine graphene. Therefore, to fully exploit graphene's potential in the device arena, we studied the effect of substrate on the non -equilibrium dynamics of carriers and phonons.

Using ultrafast degenerate pump probe spectroscopy, we first characterized the vastly diverse hot carrier induced dynamics of electrons and phonons in single layer CVD graphene transferred onto single crystal (100) diamond, quartz and sapphire.

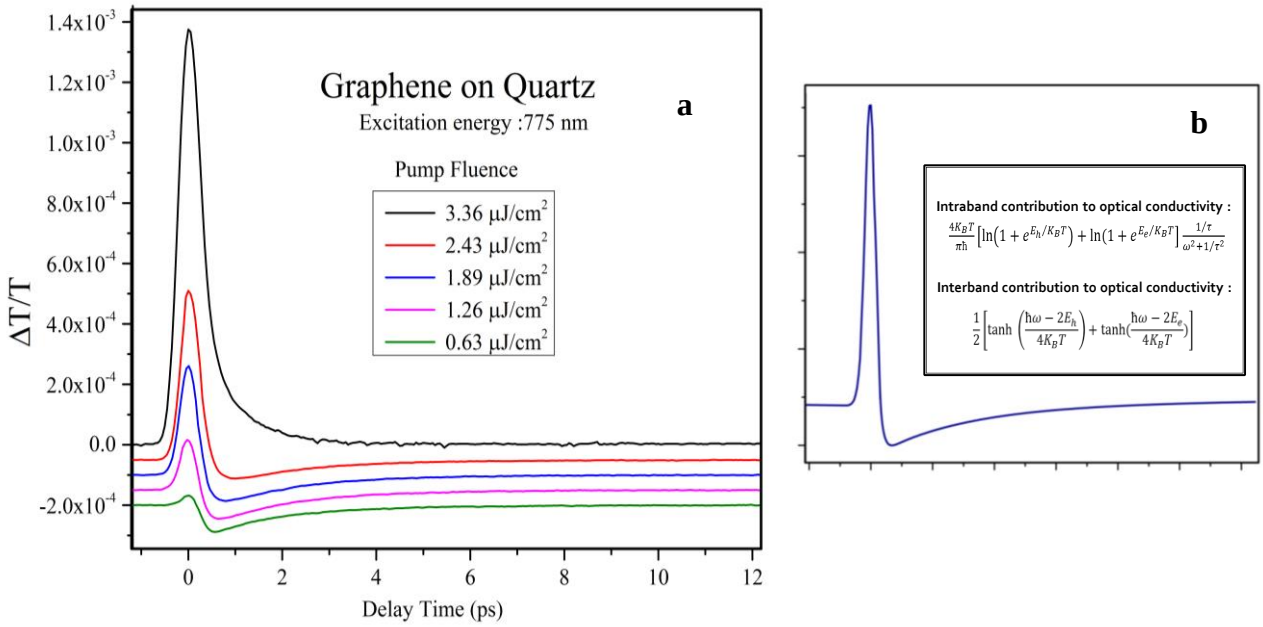

Figure 17 (a) Fluence dependent transient transmission of graphene transferred on quartz in the first 10 ps after photoexcitation. (b) Simulated transient transmission taking into account both the inter and intraband contributions to the optical conductivity of graphene.

Figure 17a) shows the fluence dependent ultrafast transient transmission for graphene transferred on quartz. The observed dynamical response can be explained using a competing inter-intra band transition model Figure 17b) where the increase in transmission is attributed to the Pauli blocking or bleaching of transitions and the subsequent decrease in transmission with much slower recovery is attributed to the intraband or Drude like scattering which is assisted by the phonons. As the pump fluence or number of photoexcited electrons increases, the band filling effects or Pauli blocking becomes more and more dominant, over shadowing the intraband contribution.

Effect of substrate in the non-equilibrium dynamics, created by pump probe spectroscopy which is similar to those experienced in FETs, is deemed to be mostly in the later stages of energy

relaxation (hundreds of picoseconds) through acoustic phonon and heat transfer between graphene and the substrate and specifically not in the early 10 ps time window where the electrons are the main carriers of energy.
Our breakthrough results show that unlike present prevailing opinion in the literature [33], in the first few ps after photoexcitation, the ultrafast dynamics of graphene highly depends on the substrate on which it resides.

As seen in Figure 18, the ultrafast relaxation of carriers in graphene on different substrates is not only different in terms of decay times but it also exhibits distinct differences in the intra and interband contributions. To explain the observed differences, we are currently working on a model which takes into account not only the electron-electron and electron- optical phonon energy relaxation pathways in graphene but also considers a much less studied relaxation channel which involves carriers of graphene directly coupling to the polar phonons of the substrate. The strength of this coupling would be different depending on the surface phonon energies available and the polarity of the substrate.

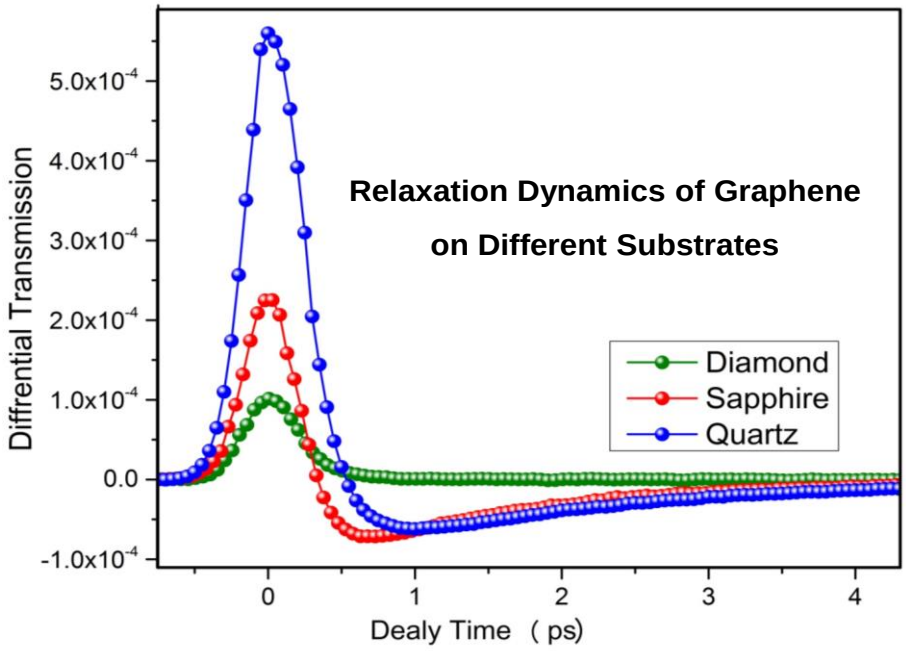

Figure 18 Figure 2. Substrate dependent transient transmission dynamics of single layer graphene pumped at 800 nm

Understanding how the relaxation dynamics of hot carriers in graphene is altered by coupling to different substrates, and deciphering the efficiency of different scattering mechanisms and different energy relaxation pathways involved, will pave the way towards realization of higher performance graphene electronic and optoelectronics.

e) Order/disorder (defects, strain and impurities) in a material as a function of depth using depth-dependent second harmonic generation (SHG)

The use of femtosecond laser pulses to characterize and control material properties at the quantum level has led to exciting developments at the frontier of condensed-matter physics. This

novel depth-dependent characterization set of experiments can accurately examine order/disorder effect (produced by defects, dopants, dynamic strain, etc.) versus depth. Using second harmonic generation (SHG), which is a direct measurement of second order non-linear susceptibility, we are able to extract elements of the photoelastic and strain tensors under transient elastic strain and their respective effect on the material's electronic structure. This technique has a spatial resolution on the order of tens of nanometers, is noninvasive and nondestructive, and is conducive to integration into fabrication processes. This technique will be particularly useful in thin film growth processes and the determination of the quality of material structures used in optoelectronic industry, where lateral dimensions are on the order of microns, but depth dimensions are on the order of tens of nanometers.

Coherent acoustic phonons (CAP) have been used for material characterization in the fields of picosecond acoustics, picosecond ultrasonics, and coherent acoustic phonon spectroscopy for several decades. The process for generating coherent acoustic phonons has been verified and well understood with ultrafast pump-probe technique [34]. Our experimental setup is presented in Figure 19. In this arrangement, a laser beam is split into two beams with 50% as the pump beam and 50% as the probe beam. When the pump beam pulse with width ~10 μm and energy of ~ 1 nJ strikes the sample, the 5-10 nm thick transducing layer expands thermally. This expansion quickly generates an acoustic pulse tens of nanometers wide, which propagates through the sample. This acoustic pulse can have a strain amplitude up to 10^{-3}. This strain amplitude is an order of magnitude *higher* than strain proven in the literature to contribute to SHG enhancement. Figure 20 shows a theoretical shape of the pump beam, which spatial size of the order of thickness of the transducing layer and a cartoon of crystal lattice modification by CAP wave. A probe beam arrives sometime later, interacting with the strain wave. The probe power is increased to create second harmonic generation (SHG) in the target material if it has an intrinsic $\chi^{(2)}$ or inherent broken centrosymmetry, a condition of SHG. In this way, the probe power monitors the change in $\chi^{(2)}$ or centrosymmetry caused by an coherent acoustic wave induced by the pump beam. These waves have produced a degree of SHG enhancement in preliminary measurements. The relative arrival time at the sample between the two pulses depends on the position of the delay stage. By varying the optical delay line, one can track the optical reflectivity variation as a function of the position (depth) of the acoustic strain into the material. A portion of the probe beam reflects off of the transducing layer and another portion off of the traveling acoustic strain wave. This causes the two probe beam linear reflections interfering destructively or constructively, producing oscillations in the optical reflectivity, which are typically collected in a detector (PD or PMT). We use two detection systems: photomultiplier combined with a photon counter to detect total SHG signal and photomultiplier combined with a lock-in amplifier working at the pump frequency to collect only the SHG signal generated by transient, dynamic strain (CAP pulse).

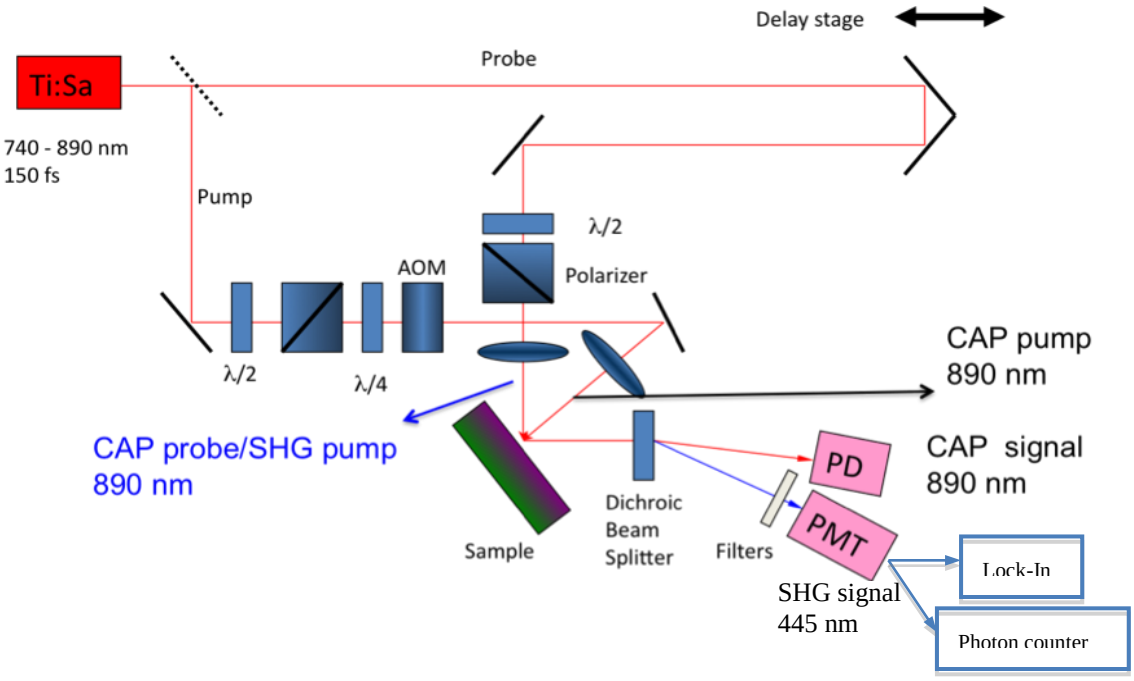

Figure 19 Experimental setup for measuring order/disorder properties in a material as a function of depth using depth-dependent second harmonic generation (SHG); AOM – acousto-optic modulator, λ/2, λ/4 – half and quarter wave plate, respectively, PD – photo detector, PMT – photomultiplier

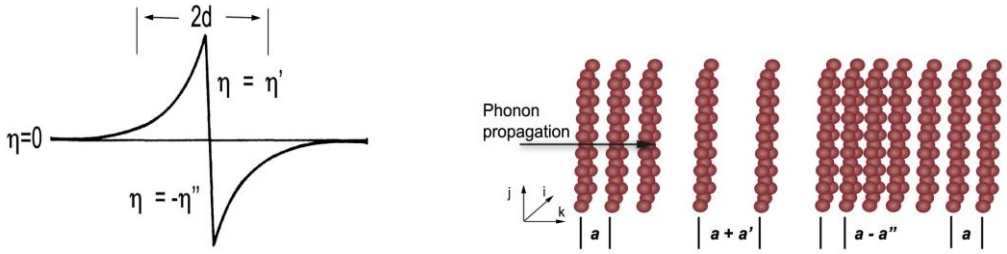

a) ***b)***

Figure 20(a) Theoretical shape of a coherent acoustic pulse, where 2d defines the spatial size of the pulse and h represents elastic strain component [35]. (b) Modification of crystal lattice due to transient strain caused by coherent acoustic phonon wave. The coherent pulses interact with the material firstly compress and subsequently tensile the crystal lattice, thereby providing additional, dynamic strain components to photo-elastic tensor.

When two photons of frequency ω are destroyed, a photon of frequency 2 ω (second harmonic photon) is subsequently emitted. The measured second harmonic intensity from the material is expressed by:

$$I_{SHG} \propto \left| P^{(2)}(2\omega) \right|^2$$

where $P^{(2)}$ is the second order nonlinear polarizability. The second order nonlinear polarizability is described by:

$$P^{(2)} = \square_0 \square^{(2)} \boldsymbol{E^2}$$

where e_0 is the permittivity of free space, $c^{(2)}$ is the second order nonlinear susceptibility tensor and *E* is electric field.

Our measurements were taken at room temperature on a GaAs substrate with 20 nm GaSb transducing layer. The laser used to excite the sample was a Coherent Mira laser set to 885 nm, which is just below the band gap of GaAs (877 nm) to prevent carrier excitation in GaAs. The resulting probe beam was sent through a dichroic beam splitter, transmitting the fundamental beam to a static semiconductor detector and reflecting the SHG beam into a PMT. The delay stage was fixed to particular relative arrival times to observe the change in SHG caused by a coherent acoustic pulse located at specific depths in the material. The SHG spectra were observed at the following depths below the free surface: 200 nm, 400 nm, 600 nm and 800 nm. These were compared to the SHG response when there was no acoustic pulse (no pump spectrum in the Figure 21) and also when the CAP was created at the free surface (0 ps spectrum in Figure 21). The responses of p-polarized pump, p-polarized probe and s-polarized SHG collection (PPS) and p-polarized pump, p-polarized probe and p-polarized SHG collection (PPP) are shown in the figure below.

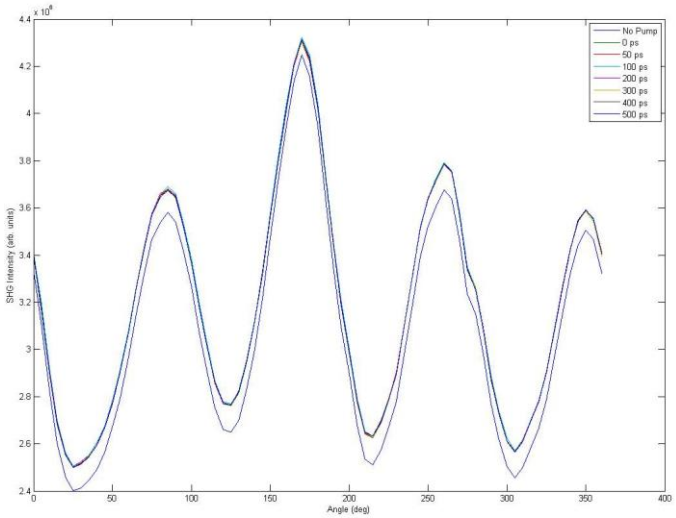

Figure 21 Fourfold symmetry SHG diagrams collected by a PMT and photon counter system containing the total second harmonic response from the sample.

The total enhancement of the SHG signal, shown in Figure 21, is related to at least three contributions: point defects, lattice mismatch (in the case of multilayer structures) and transient strain caused by moving CAP. The areas in tension or compression (produced by CAP) change the lattice symmetry locally (see Figure 20b). Owing to this technique we are able to measure depth-dependent SHG created only by CAP wave with accuracy of tents of nm. Figure 22 presents changes of the separated second harmonic signal produced **only** by transient ultrafast pulse, dependent on azimuth angle. That means, we are able to follow any dynamic changes in the crystal symmetry with nm resolution. Information extracted from the measurements will be compared to a phenomenological model of SHG signal as well as by density functional theory (DFT) calculations.

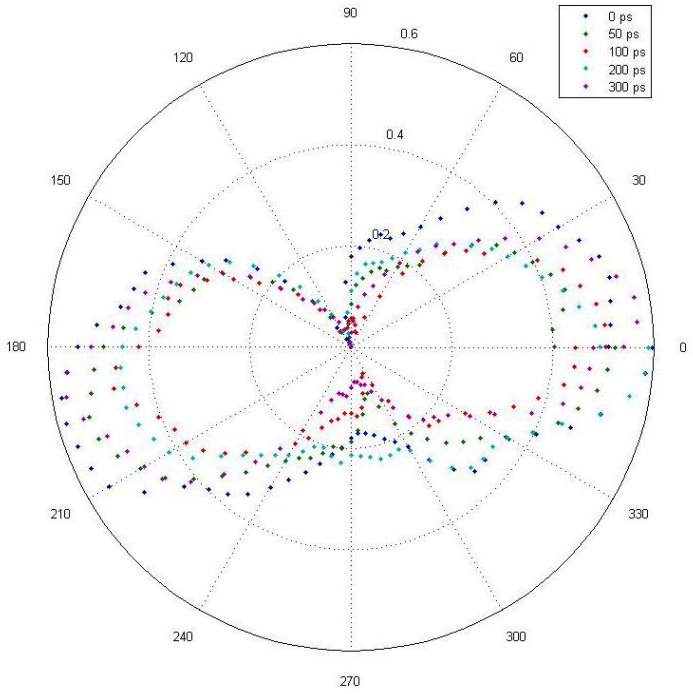

Figure 22 Twofold symmetry SHG polar diagrams collected by PMT and Lock-In containing only second harmonic response from CAP transient strain

The target materials for this patent are as follows: GaAs, GaSb/GaAs, Si, SiO_2/Si and silicon on insulator (SOI). The underlying physics of the CAP/SHG technique rely on the distortion of the material's local electronic structure through transient lattice strain caused by CAP. In areas of significant strain, the photoelastic constant is reduced, causing a change in the amount of probe light reflected at the traveling interface. This allows for measurement of any subsurface feature that induces strain, including intentional dopants, impurities, interfaces, interfacial strain arising from lattice mismatch and defect complexes.

This CAP/SHG method has the potential to radically improve ability to identify and quantify order/disorder effect due to defects and transient strain at reduced cost and labor. In order to help translate our technology to useful industrial applications we have identified four areas of development to be investigated in our proposed study. These are *spatial resolution, defect sensitivity, determination of defect type, electronic structure effects:*

(1) *Spatial resolution* – One of the primary aspects of materials characterization is how well and on what size scale features can be resolved. We intend to carry out a systematic study on both III-V materials (e.g. GaSb/GaAs) and SiO_2/Si structures. Currently, it is believed that the ultimate spatial resolution is on the order of twice the material's optical penetration depth (~10 nm).

(2) *Sensitivity* – The SHG technique is also extremely sensitive to various types of defect concentrations. Current experiments indicate that the technique is capable to measure electric fields as low as 10^3 V/m, which is not achievable by the other techniques.

(3) *Determination of disorder type* – One of the most useful/powerful aspects of the combined CAP/SHG technique is its dependence on changes of crystal electric field and in consequence, strain tensor components of the material. As various crystal structure modifications (including crystal imperfections like dislocations, lattice mismatch, implanted dopants, etc.) have different SHG response at different depth. By repeating the CAP/SHG measurement as the time delay between pump and probe beam we are able to achieve the complete strain/dislocation depth profile of the target.

(4) *Electronic structure effects* – Additionally, the reflection of the CAP probe light is primarily dependent on the local electronic structure surrounding the defects. This provides a convenient path to studying the complex interplay between defect strain and electronic structure distortion, including how many lattice points per defect are influenced.

Currently we have provided a proof-of-principle demonstration that CAP wave can allow us to accurately measure depth-dependent polar SHG profiles in a way not possible by any other technique. The above points provide a roadmap for making the technique a competitive characterization method, with great potential for industrial application.
This new approach constitutes a totally new approach to measure any strain, dopants, impurities, interfaces and interfacial strain arising from lattice deformation as a function of depth. This is a capability that is of great importance to the semiconductor device community as it provides a means of *in-situ* quality control.

V. BES (DoE) supported patents

1. A. Baydin, J.L. Davidson, H. Krzyzanowska, N.H. Tolk, *A novel method for depth-dependent transient and permanent materials modification utilizing ultrafast lasers induced band gap narrowing*, Vanderbilt University, U.S. Patent Office, serial number 62/199,806, July 31, 2015

2. J. Garnett, H. Krzyżanowska, N.H. Tolk, *A novel method for measuring order/disorder (defects, strain and impurities) in a material as a function of depth using depth-dependent second harmonic generation (SHG)*, Vanderbilt University, U.S. Patent Office, serial number 62/023,078, July 11, 2014

VI. BES (DoE) supported publication list

[1] M. Budde, G. Lüpke, C. Parks Cheney, N. H. Tolk, and L. C. Feldman, "Vibrational Lifetime of Bond-Center Hydrogen in Crystalline Silicon," Phys. Rev. Lett., vol. 85, no. 7, pp. 1452–1455, Aug. 2000.
[2] M. Budde, B. Bech Nielsen, C. Parks Cheney, N. H. Tolk, and L. C. Feldman, "Local Vibrational Modes of Isolated Hydrogen in Germanium," Phys. Rev. Lett., vol. 85, no. 14, pp. 2965–2968, Oct. 2000.
[3] M. Budde, C. Parks Cheney, G. Lüpke, N. H. Tolk, and L. C. Feldman, "Vibrational dynamics of bond-center hydrogen in crystalline silicon," Phys. Rev. B, vol. 63, no. 19, p. 195203, Apr. 2001.

[4] M. Budde, G. Lüpke, E. Chen, X. Zhang, N. H. Tolk, L. C. Feldman, E. Tarhan, A. K. Ramdas, and M. Stavola, "Lifetimes of Hydrogen and Deuterium Related Vibrational Modes in Silicon," Phys. Rev. Lett., vol. 87, no. 14, p. 145501, Sep. 2001.
[5] G. Lüpke, X. Zhang, B. Sun, A. Fraser, N. H. Tolk, and L. C. Feldman, "Structure-Dependent Vibrational Lifetimes of Hydrogen in Silicon," Phys. Rev. Lett., vol. 88, no. 13, p. 135501, Mar. 2002.
[6] C. Parks Cheney, M. Budde, G. Lüpke, L. C. Feldman, and N. H. Tolk, "Vibrational dynamics of isolated hydrogen in germanium," Phys. Rev. B, vol. 65, no. 3, p. 035214, Jan. 2002.
[7] L. FELDMAN, G. LPKE, N. TOLK, R. LOPEZ, R. HAGLUND, T. HAYNES, and L. BOATNER, "Particle–solid interactions and 21st century materials science," Nucl. Instruments Methods Phys. Res. Sect. B Beam Interact. with Mater. Atoms, vol. 212, pp. 1–7, Dec. 2003.
[8] G. Lüpke, N. H. Tolk, and L. C. Feldman, "Vibrational lifetimes of hydrogen in silicon," J. Appl. Phys., vol. 93, no. 5, p. 2317, 2003.
[9] B. Sun, Q. Yang, R. C. Newman, B. Pajot, N. H. Tolk, L. C. Feldman, and G. Lüpke, "Vibrational Lifetimes and Isotope Effects of Interstitial Oxygen in Silicon and Germanium," Phys. Rev. Lett., vol. 92, no. 18, p. 185503, May 2004.
[10] B. Sun, G. A. Shi, S. V. S. Nageswara Rao, M. Stavola, N. H. Tolk, S. K. Dixit, L. C. Feldman, and G. Lüpke, "Vibrational Lifetimes and Frequency-Gap Law of Hydrogen Bending Modes in Semiconductors," Phys. Rev. Lett., vol. 96, no. 3, p. 035501, Jan. 2006.
[11] S. V. S. Nageswara Rao, S. K. Dixit, G. Lüpke, N. H. Tolk, and L. C. Feldman, "Effect of energetic ions on the stability of bond-center hydrogen in silicon," Phys. Rev. B, vol. 75, no. 23, p. 235202, Jun. 2007.
[12] X. Lu, R. Pasternak, H. Park, J. Qi, N. H. Tolk, A. Chatterjee, R. D. Schrimpf, and D. M. Fleetwood, "Temperature-dependent second- and third-order optical nonlinear susceptibilities at the SiÕSiO2 interface," Phys. Rev. B, vol. 78, no. 15, p. 155311, Oct. 2008.
[13] H. Park, J. Qi, Y. Xu, K. Varga, S. M. Weiss, B. R. Rogers, G. Lüpke, and N. Tolk, "Characterization of boron charge traps at the interface of Si/SiO2 using second harmonic generation," Appl. Phys. Lett., vol. 95, no. 6, p. 062102, Aug. 2009.
[14] A. Steigerwald, Y. Xu, J. Qi, J. Gregory, X. Liu, J. K. Furdyna, K. Varga, A. B. Hmelo, G. Lüpke, L. C. Feldman, and N. Tolk, "Semiconductor point defect concentration profiles measured using coherent acoustic phonon waves," Appl. Phys. Lett., vol. 94, no. 11, p. 111910, 2009.
[15] P. N. Ciesielski, C. J. Faulkner, M. T. Irwin, J. M. Gregory, N. H. Tolk, D. E. Cliffel, and G. K. Jennings, "Enhanced Photocurrent Production by Photosystem I Multilayer Assemblies," Adv. Funct. Mater., vol. 20, no. 23, pp. 4048–4054, Dec. 2010.
[16] H. Park, Y. Xu, K. Varga, J. Qi, L. C. Feldman, G. Lüpke, and N. Tolk, "Photon energy threshold for filling boron induced charge traps in SiO2 near the Si/SiO2 interface using second harmonic generation," Appl. Phys. Lett., vol. 97, no. 20, p. 202105, 2010.
[17] J. Qi, J. A. Yan, H. Park, A. Steigerwald, Y. Xu, S. N. Gilbert, X. Liu, J. K. Furdyna, S. T. Pantelides, and N. Tolk, "Mechanical and electronic properties of ferromagnetic Ga1−xMnxAs using ultrafast coherent acoustic phonons," Phys. Rev. B, vol. 81, no. 11, p. 115208, Mar. 2010.
[18] E. J. Spahr, L. Wen, M. Stavola, L. A. Boatner, L. C. Feldman, N. H. Tolk, and G. Lüpke, "Giant Enhancement of Hydrogen Transport in Rutile TiO2 at Low Temperatures," Phys. Rev. Lett., vol. 104, no. 20, p. 205901, May 2010.

[19] S. V. S. Nageswara Rao, S. K. Dixit, G. Lüpke, N. H. Tolk, and L. C. Feldman, "Reconfiguration and dissociation of bonded hydrogen in silicon by energetic ions," Phys. Rev. B, vol. 83, no. 4, p. 045204, Jan. 2011.
[20] H. Park, J. Qi, Y. Xu, G. Lüpke, and N. Tolk, "Polarization-dependent temporal behaviour of second harmonic generation in Si / SiO 2 systems," J. Opt., vol. 13, no. 5, p. 055202, May 2011.
[21] J. Gregory, A. Steigerwald, H. Takahashi, A. Hmelo, and N. Tolk, "Ion implantation induced modification of optical properties in single-crystal diamond studied by coherent acoustic phonon spectroscopy," Appl. Phys. Lett., vol. 101, no. 18, p. 181904, 2012.
[22] a. Steigerwald, a. B. Hmelo, K. Varga, L. C. Feldman, and N. Tolk, "Determination of optical damage cross-sections and volumes surrounding ion bombardment tracks in GaAs using coherent acoustic phonon spectroscopy," J. Appl. Phys., vol. 112, no. 1, p. 013514, 2012.
[23] H. Park, B. Choi, A. Steigerwald, K. Varga, and N. Tolk, "Annealing effect in boron-induced interface charge traps in Si/SiO2 systems," J. Appl. Phys., vol. 113, no. 2, p. 023711, 2013.
[24] H. Park, J. Qi, Y. Xu, G. Lüpke, and N. Tolk, "Corrigendum: Polarization-dependent temporal behaviour of second harmonic generation in Si/SiO2 systems," J. Opt., vol. 15, no. 7, p. 079501, Jul. 2013.
[25] H. M. Lawler, A. Steigerwald, J. Gregory, H. Krzyzanowska, and N. H. Tolk, "Experimental and theoretical determination of the opto-acoustic spectrum of silicon," Mater. Res. Express, vol. 1, no. 2, p. 025701, Apr. 2014.
[26] A. R. Klots, A. K. M. Newaz, B. Wang, D. Prasai, H. Krzyzanowska, J. Lin, D. Caudel, N. J. Ghimire, J. Yan, B. L. Ivanov, K. A. Velizhanin, A. Burger, D. G. Mandrus, N. H. Tolk, S. T. Pantelides, and K. I. Bolotin, "Probing excitonic states in suspended two-dimensional semiconductors by photocurrent spectroscopy," Sci. Rep., vol. 4, p. 6608, Oct. 2014.
[27]. S. Gilbert Corder, J. Kawasaki, Ch. Palmstrom, H. Krzyżanowska, N. Tolk, Effects of nanoscale embedded Schottky barriers on carrier dynamics in ErAs:GaAs composite systems, accepted to *Phys. Rev. B*, September 2015
[28] S. N. Gilbert Corder, H. Krzyzanowska, J. Kawasaki, C. Palmstrom, and N. Tolk, "Strong surface plasmon effects in ErAs:GaAs composite systems in the GHz frequency range," to be submitted to Physical Review B (2015)
[29] S. N. Gilbert Corder, H. Krzyzanowska, J. Kawasaki, C. Palmstrom, and N. Tolk, "Strong surface plasmon effects in ErAs:GaAs composite systems in the GHz frequency range," to be submitted to Physical Review B (2015)
[30] Andrey Baydin, Halina Krzyzanowska, Leonard Feldman, Norman Tolk, Strong optical response form H^+ implanted 4H-SiC at low doses optical constants of H^+ damaged n-type 4H-SiC, to be submitted to Applied Physics Letters (2015)

VII. Conclusion

In this report, we have chronicled a broad, ambitious and successful research program for the study of interactions involving electron and phonon excitation of defects, dopants, and interfaces in semiconducting crystals. We have made measurements in the ultrafast regime, representing far-from-equilibrium conditions where the electronic and lattice systems have not had sufficient time to thermalize. We have also investigated confined electronic systems, such as the two-dimensional electron gas. Such research directions open the exciting possibility for coherent

quantum-level control of materials. It is clear that this work relates directly to the mission of the Department of Energy. Knowledge of the rates and pathways of vibrational energy flow in condensed matter is critical for understanding dynamical processes in solids including electronically, optically and thermally stimulated defect and impurity reactions and migration. The ability to directly probe these pathways and rates allows tests of theory and scaling laws at new levels of precision. These basic dynamical studies have provided new insights, for example, into the fundamental mechanisms that control energy flow and atom diffusion in oxides and semiconductors. And importantly, it provides the framework for innovative new approaches to the manipulation and modification of matter in a spatially localized and non-thermal manner.

VIII. Bibliography

[1] M. Budde, G. Lupke, C. P. Cheney, N. H. Tolk, and L. C. Feldman, "Vibrational lifetime of bond-center hydrogen in crystalline silicon," *Phys. Rev. Lett.*, vol. 85, no. 7, pp. 1452–9007, 2000.

[2] M. Budde, B. Bech Nielsen, C. Parks Cheney, N. H. Tolk, and L. C. Feldman, "Local Vibrational Modes of Isolated Hydrogen in Germanium," *Phys. Rev. Lett.*, vol. 85, no. 14, pp. 2965–2968, Oct. 2000.

[3] M. Budde, C. Parks Cheney, G. Lüpke, N. H. Tolk, and L. C. Feldman, "Vibrational dynamics of bond-center hydrogen in crystalline silicon," *Phys. Rev. B*, vol. 63, no. 19, p. 195203, Apr. 2001.

[4] C. Parks Cheney, M. Budde, G. Lüpke, L. C. Feldman, and N. H. Tolk, "Vibrational dynamics of isolated hydrogen in germanium," *Phys. Rev. B*, vol. 65, no. 3, p. 035214, Jan. 2002.

[5] G. Lüpke, X. Zhang, B. Sun, A. Fraser, N. H. Tolk, and L. C. Feldman, "Structure-Dependent Vibrational Lifetimes of Hydrogen in Silicon," *Phys. Rev. Lett.*, vol. 88, no. 13, p. 135501, Mar. 2002.

[6] G. Lupke, N. H. Tolk, and L. C. Feldman, "Vibrational lifetimes of hydrogen in silicon," *J. Appl. Phys.*, vol. 93, no. 5, pp. 2317–8979, 2003.

[7] L. Feldman, G. Lpke, N. Tolk, R. Lopez, R. Haglund, T. Haynes, And L. Boatner, "Particle–solid interactions and 21st century materials science," *Nucl. Instruments Methods Phys. Res. Sect. B Beam Interact. with Mater. Atoms*, vol. 212, pp. 1–7, Dec. 2003.

[8] B. Sun, Q. Yang, R. C. Newman, B. Pajot, N. H. Tolk, L. C. Feldman, and G. Lüpke, "Vibrational Lifetimes and Isotope Effects of Interstitial Oxygen in Silicon and Germanium," *Phys. Rev. Lett.*, vol. 92, no. 18, p. 185503, May 2004.

[9] L. C. Feldman, G. Lüpke, and N. H. Tolk, "Vibrational Lifetimes of Hydrogen and Silicon MOSFET Reliability," *Solid State Phenom.*, vol. 95–96, pp. 123–128, 2004.

[10] L. Hsu, M. D. McCluskey, and J. L. Lindström, "Resonant Interaction between Localized and Extended Vibrational Modes in Si: O18 under Pressure," *Phys. Rev. Lett.*, vol. 90, no. 9, p. 095505, Mar. 2003.

[11] J. Kato, K. M. Itoh, H. Yamada-Kaneta, and H.-J. Pohl, "Host isotope effect on the localized vibrational modes of oxygen in isotopically enriched 28Si, 29Si, and 30Si single crystals," *Phys. Rev. B*, vol. 68, no. 3, p. 35205, Jul. 2003.

[12] A. Facchetti and T. J. Marks, *Transparent Electronics: From Synthesis to Applications*. 2010.

[13] A. K. Singh, A. Janotti, M. Scheffler, and C. G. de Walle, "Sources of Electrical Conductivity in SnO2," *Phys. Rev. Lett.*, vol. 101, no. 5, p. 55502, Jul. 2008.

[14] G. A. Shi, M. Saboktakin, M. Stavola, and S. J. Pearton, "'Hidden hydrogen' in as-grown ZnO," *Appl. Phys. Lett.*, vol. 85, no. 23, p. 5601, Dec. 2004.

[15] W. M. Hlaing Oo, S. Tabatabaei, M. D. McCluskey, J. B. Varley, A. Janotti, and C. G. Van de Walle, "Hydrogen donors in SnO 2 studied by infrared spectroscopy and first-principles calculations," *Phys. Rev. B*, vol. 82, no. 19, p. 193201, Nov. 2010.

[16] E. J. Spahr, L. Wen, M. Stavola, L. A. Boatner, L. C. Feldman, N. H. Tolk, and G. Lüpke, "Proton tunneling: A decay channel of the O-H stretch mode in KTaO3," *Phys. Rev. Lett.*, vol. 102, no. 7, p. 075506, Feb. 2009.

[17] I. Kuskovsky, B. Lim, and A. Nowick, "Low-temperature dielectric relaxation peaks involving proton tunneling in Ba1-xNdxCeO3," *Physical Review B*, vol. 60, no. 6. pp. R3713–R3715, 1999.

[18] M. Budde, G. Lüpke, E. Chen, X. Zhang, N. H. Tolk, L. C. Feldman, E. Tarhan, A. K. Ramdas, and M. Stavola, "Lifetimes of Hydrogen and Deuterium Related Vibrational Modes in Silicon," *Phys. Rev. Lett.*, vol. 87, no. 14, p. 145501, Sep. 2001.

[19] A. Steigerwald, Y. Xu, J. Qi, J. Gregory, X. Liu, J. K. Furdyna, K. Varga, a. B. Hmelo, G. Lüpke, L. C. Feldman, N. Tolk, G. Lüpke, L. C. Feldman, and N. Tolk, "Semiconductor point defect concentration profiles measured using coherent acoustic phonon waves," *Appl. Phys. Lett.*, vol. 94, no. 11, p. 111910, 2009.

[20] A. Steigerwald, A. B. Hmelo, K. Varga, L. C. Feldman, and N. Tolk, "Determination of optical damage cross-sections and volumes surrounding ion bombardment tracks in GaAs using coherent acoustic phonon spectroscopy," *J. Appl. Phys.*, vol. 112, 2012.

[21] H. Park, B. Choi, A. Steigerwald, K. Varga, and N. Tolk, "Annealing effect in boron-induced interface charge traps in Si/SiO2 systems," *J. Appl. Phys.*, vol. 113, no. 2, p. 023711, 2013.

[22] W. F. Paxton, M. M. Brooks, M. Howell, N. Tolk, W. P. Kang, and J. L. Davidson, "Role of deuterium desorption kinetics on the thermionic emission properties of polycrystalline diamond films with respect to kinetic isotope effects," *J. Appl. Phys.*, vol. 115, no. 23, p. 234904, 2014.

[23] J. Gregory, A. Steigerwald, H. Takahashi, A. Hmelo, and N. Tolk, "Ion implantation induced modification of optical properties in single-crystal diamond studied by coherent acoustic phonon spectroscopy," *Appl. Phys. Lett.*, vol. 101, pp. 1–14, 2012.

[24] H. M. Lawler, a Steigerwald, J. Gregory, H. Krzyzanowska, and N. H. Tolk, "Experimental and theoretical determination of the opto-acoustic spectrum of silicon," *Mater. Res. Express*, vol. 1, no. 2, p. 025701, 2014.

[25] D. D. Nolte, "Optical scattering and absorption by metal nanoclusters in GaAs," *J. Appl. Phys.*, vol. 76, no. 6, pp. 3740–3745, 1994.

[26] M. P. Hanson, A. C. Gossard, and E. R. Brown, "Infrared surface plasmon resonances due to Er-V semimetallic nanoparticles in III-V semiconductor matrices," *J. Appl. Phys.*, vol. 102, no. 4, 2007.

[27] R. P. Prasankumar, A. Scopatz, D. J. Hilton, A. J. Taylor, R. D. Averitt, J. M. Zide, and A. C. Gossard, "Carrier dynamics in self-assembled ErAs nanoislands embedded in GaAs measured by optical-pump terahertz-probe spectroscopy," *Appl. Phys. Lett.*, vol. 86, no. 20, pp. 1–3, 2005.

[28] E. R. Brown, A. Bacher, D. Driscoll, M. Hanson, C. Kadow, and A. C. Gossard, "Evidence for a strong surface-plasmon resonance on ErAs nanoparticles in GaAs.," *Phys. Rev. Lett.*, vol. 90, no. 7, p. 077403, 2003.

[29] J. K. Kawasaki, R. Timm, K. T. Delaney, E. Lundgren, A. Mikkelsen, and C. J. Palmstrøm, "Local Density of States and Interface Effects in Semimetallic ErAs Nanoparticles Embedded in GaAs," *Phys. Rev. Lett.*, vol. 107, no. 3, p. 036806, Jul. 2011.

[30] M. a. Scarpulla, J. M. O. Zide, J. M. LeBeau, C. G. Van De Walle, A. C. Gossard, and K. T. Delaney, "Near-infrared absorption and semimetal-semiconductor transition in 2 nm ErAs nanoparticles embedded in GaAs and AlAs," *Appl. Phys. Lett.*, vol. 92, pp. 2008–2010, 2008.

[31] C. Kadow, S. B. Fleischer, J. P. Ibbetson, J. E. Bowers, A. C. Gossard, J. W. Dong, Palmstr, oslash, and C. J. m, "Self-assembled ErAs islands in GaAs: Growth and subpicosecond carrier dynamics," *Appl. Phys. Lett.*, vol. 75, no. 22, pp. 3548–3550, 1999.

[32] I. Meric, M. Y. Han, A. F. Young, B. Ozyilmaz, P. Kim, and K. L. Shepard, "Current saturation in zero-bandgap, top-gated graphene field-effect transistors.," *Nat. Nanotechnol.*, vol. 3, no. 11, pp. 654–659, 2008.

[33] H. Wang, J. H. Strait, P. a. George, S. Shivaraman, V. B. Shields, M. Chandrashekhar, J. Hwang, F. Rana, M. G. Spencer, C. S. Ruiz-Vargas, and J. Park, "Ultrafast relaxation dynamics of hot optical phonons in graphene," *Appl. Phys. Lett.*, vol. 96, no. 8, pp. 2013–2016, 2010.

[34] C. Thomsen, J. Strait, Z. Vardeny, H. J. Maris, J. Tauc, and J. J. Hauser, "Coherent phonon generation and detection by picosecond light pulses," *Phys. Rev. Lett.*, vol. 53, no. 10, pp. 989–992, 1984.

[35] O. Matsuda, O. B. Wright, D. H. Hurley, V. Gusev, and K. Shimizu, "Coherent shear phonon generation and detection with picosecond laser acoustics," *Phys. Rev. B - Condens. Matter Mater. Phys.*, vol. 77, pp. 1–16, 2008.